A&A 460, 821–829 (2006)
DOI: 10.1051/0004-6361:20065160

Astronomy & Astrophysics

Fe II emission lines in Be stars

I. Empirical diagnostic of physical conditions in the circumstellar discs*

M. L. Arias[1,3,**], J. Zorec[2], L. Cidale[1,3], A. E. Ringuelet[1], N. I. Morrell[4], and D. Ballereau[5]

[1] Facultad de Ciencias Astronómicas y Geofísicas, Universidad Nacional de La Plata, Paseo del Bosque s/n, (1900) La Plata, Argentina
e-mail: mlaura@fcaglp.fcaglp.unlp.edu.ar
[2] Institut d'Astrophysique de Paris, UMR7095 CNRS, Université Pierre & Marie Curie, 98bis Bd. Arago, 75014 Paris, France
[3] Instituto de Astrofísica de La Plata (CONICET-UNLP), Paseo del Bosque s/n, (1900) La Plata, Argentina
[4] Las Campanas Observatory, Carnegie Observatories, Casilla 601, La Serena, Chile
[5] GEPI, UMR 8111 du CNRS, Observatoire de Paris-Meudon, 92195 Meudon Cedex, France

Received 8 March 2006 / Accepted 22 June 2006

ABSTRACT

Aims. The Fe II emission lines formed in the circumstellar envelopes (CE) of classical Be stars are studied in order to determine whether they are optically thin or optically thick. We also aim at deriving both average Fe II line excitation temperatures and the extent of their formation region in the CE.

Methods. We simultaneously observed several series of Fe II emission lines in the $\lambda\lambda$4230–7712 Å wavelength interval and the first members of the hydrogen Balmer series of 18 southern classical Be stars. The optical depth regime that controls the formation of the observed Fe II lines and the physical parameters of their CE formation region were studied using the empirical self-aborption-curve (SAC) method.

Results. Our calculations give an average value of $\tau_o = 2.4 \pm 0.9$ for the optical depth of the studied Fe II lines, which implies that these lines are optically thick in the CE of Be stars. Qualitative indications that Fe II emission lines should be formed in circumstellar regions close to the central star are inferred from the correlations between Fe II emission line widths and $V \sin i$. The application of the SAC method to Fe II emission lines confirms this result, which gives $R_e = 2.0R_* \pm 0.8$ for the extension of the line-forming region. The proximity of the line-forming region to the central star is also supported by the behavior of the source function of Fe II lines, which rapidly decreases with radii. This prevents the lines from being formed over extended regions and/or far from the star. Finally, the correlations of the central depression in the Balmer emission lines with $V \sin i$ are consistent with the flattened geometrical shapes of CEs.

Key words. stars: emission-line, Be – stars: circumstellar matter – line: profiles – line: formation

1. Introduction

The ionization potential of neutral Fe is 7.8 eV, while that of Fe II ions is 16.2 eV. This implies that due to the average excitation conditions that exist in the atmospheric and exophotospheric regions of a wide variety of stellar objects, iron is present mainly in the Fe II ionization state. In fact, Fe II lines are observed in the Sun, in Be stars and other objects with the B[e] phenomenon, Be/X stars, LBV, cataclysmic variables, cool variables, novae, supernova remnants, H II regions, planetary nebulae, AGN, quasars, etc.

Although the Grotrian diagram of the Fe II ion is quite complex, its atomic levels can be classified into three categories: low even levels, metastable levels at roughly 3eV above the lower levels, and high odd levels at about 5 eV from the lower or fundamental levels. Transitions among these levels then produce spectral lines that are seen in the UV, optical, and near IR spectral region. In each case, different regions of a given environment can be responsible for the formation of the observed Fe II lines (Viotti 1976; Collin-Soufrin et al. 1979, 1980).

Emission in the first Balmer members can be seen in all sub-spectral types of Be stars, while emission in Fe II lines is mainly seen in subtypes earlier than B5 (Hubert-Delplace & Hubert 1979). Qualitative descriptions of the occurrence of Fe II lines in Be stars were made by Wellman (1952), Viotti & Koubský (1976), Geisel (1970), Allen & Swings (1976), Viotti (1976), Slettebak (1982), and Polidan & Peters (1976). Hanuschik (1987, 1988) and Ballereau et al. (1995) carried out somewhat more systematic studies, but they limited their discussion to the strongest Fe II emission lines in the visual. In these works the opacity regime that controls the formation of Fe II emission lines and the actual location and/or extent of their formation region have not been clearly established. All discussions by Hanuschik (1987, 1988) and Dachs et al. (1992) on the average kinematic properties of discs in Be stars and conclusions that Fe II lines are formed inside the Hα and Hβ emission line-formation zone are both entirely based on the assumption that Fe II lines are optically thin. In contrast, Ballereau et al. (1995) claim that Fe II lines in Be stars must be optically thick, which can lead to a somewhat different vision of the kinematics of CE and of the actual location of the formation region of these lines.

* Figures 7–17 and Tables 4–7 are only available in electronic form at http://www.aanda.org

** Visiting Astronomer of CASLEO, operated under agreement among CONICET and the National Universities of La Plata, San Juan and Córdoba, Argentina.

In general, it is thought that this region is located in the H II→H I transition region (Netzer 1988) in a wide variety of astrophysical objects. Tarafdar & Apparao (1994) argued that Fe II emission lines in Be stars cannot form in the H II region around the central object, because of its small extent.

It follows then that the location of the Fe II emission line-formation region in the CE of Be stars can be determined less ambiguously, if the optical depth regime of lines and the extent of their formation region are analyzed simultaneously. This is the precise aim of the present work. To this purpose, we used the self-absorption-curve (SAC) method developed by Friedjung & Muratorio (1987), which enabled us to determine consistently the optical depth regime of the studied lines, their average excitation temperature, and the extent of their formation region. The method is based on the use of many Fe II-line multiplets, each with many emission lines.

2. Stellar sample and observations

We carried out observations of 18 southern Be stars at the Complejo Astronómico El Leoncito (CASLEO), San Juan, Argentina in March and September 1996, using the 2.15 m telescope, a REOSC échelle Cassegrain spectrograph with a 400 mm^{-1} grating in cross dispersion and a Tek 1024 × 1024 CCD. The spectral range from 3900 Å to 8000 Å, with mean resolution $R = 11\,500$, was observed using two different tilts of the grating. Data reduction was made using the IRAF[1] software package. Most of the program objects were observed in both above-mentioned epochs.

The studied objects are classical Be stars, i.e. non-supergiant B-type stars whose spectrum has, or had at some time, one or more Balmer lines in emission (Jaschek et al. 1981; Collins 1987). All selected Be stars show significant emission in the first terms of the hydrogen Balmer series and in the Fe II lines. As indicated in the introduction, most of these stars are then hotter than spectral type B5. Table 1 lists the program stars and their fundamental parameters and gives the log of observations. Julian days and detailed spectral ranges observed are given in the online Table 4. When available, the MK spectral types and the ($\log T_{\rm eff}, \log g$) parameters are from the BCD (λ_1, D) system (Divan & Zorec 1982; Frémat et al. 2005; Zorec et al. 2005). The $V \sin i$ are from Chauville et al. (2001). The inclination angle i of each star is from Frémat et al. (2005), where this parameter was derived using models of stellar atmospheres that take into account the gravitational darkening effect induced by the geometrical distortion produced by the fast rotation of stars.

Table 1. Program stars and log of observations.

Object	Sp.T	$V \sin i$ km s^{-1}	$\log T_{\rm eff}$	$\log g$	i [deg]	Date
HD 41335	B1.5IIIne	358	4.320	3.89	69	1,2
HD 45725	B2.5IV-Ve	330	4.251	3.90	67	3
HD 48917	B2III-IVe	205	4.308	3.40	45	3
HD 50013	B1.5IVne	243	4.391	4.02	37	1,2
HD 56139	B2IVe	84	4.291	3.62	17	3
HD 58978	B0Vpe	375	4.388	4.15	55	3
HD 63462	B0Ve	435	4.424	3.60	90	1,2
HD 88661	B2IVpne	237	4.333	3.99	39	1,2
HD 91465	B3IIIne	266	4.240	3.52	67	1,2
HD 105435	B2IVne	258	4.349	3.92	42	1,2
HD 110335	B6IVe	208[a]	4.120[b]	3.28[b]	63	3
HD 112091	B5Vne	210	4.309	3.93	36	3
HD 120991	B2IIIe	70	4.347	3.69	13	1,2
HD 124367	B4IVne	295	4.243	3.76	63	1,2
HD 148184	B0.5Vpe	144	4.459	3.91	20	1,2,4
HD 157042	B2IVe	340	4.338	4.06	53	4
HD 158427	B3Vne	290	4.256	3.99	51	4
HD 164284	B2Ve	262	4.426	3.95	53	4

Dates: 1 ≡ 5 Mar. 1996, 2 ≡ 6 Mar. 1996, 3 ≡ 7 Mar. 1996, 4 ≡ 21 Sep. 1996. Julian days are given in the online Table 4. [a] Yudin (2001); [b] de Geus et al. (1989). The inclination angle i was derived using stellar atmospheres calculated for rotationally deformed and gravitationally darkened stars (Frémat et al. 2005).

3. Fe II emission line profiles

We studied several Fe II line multiplets: 27, 28, 37, 38, 48, 49, 55, 73, and 74. For rare cases, we could also measure some lines of multiplets 40, 41, and 43. In the chosen multiplets the emission is the strongest, so much easier to identify and measure. The respective basic atomic data were taken from the National Institute of Standards and Technology (NIST) database (http://physics.nist.gov/cgi-bin/AtData/main_asd) and R. L. Kurucz (1995, private communication).

Figure 1 shows line emission profiles normalized to the continuum of a sample of Fe II line multiplets observed in some Be stars. The wavelength of the plotted Fe II lines is shown in the first box of the figure. Line λ5363 corresponds to multiplet 48, while the remaining ones are of multiplet 49. Figure 1 is an excerpt of the spectroscopic data obtained. The profiles of most Fe II lines used to obtain the SAC curve of each object are available online (online Fig. 7 to Fig. 12). Although many lines were measured, not all of them are displayed in the atlas. Due to space limitations, we had to choose a layout presenting only the most outstanding among the observed transitions. All Fe II and hydrogen Balmer lines were observed simultaneously. For each star, the Balmer Hα, Hβ, and Hγ lines are also shown in Fig. 1. The online atlas of line profiles also includes the first three lines of the hydrogen Balmer series (the online Figs. 13 to 15). The velocity scales used are heliocentric.

As seen in Fig. 1, all Fe II profiles are double peaked and have a central depression whose depth and shape is different from line to line. The Fe II lines are quite weak; in general they do not rise above some 0.2 in intensity over the continuum. Contrary to the hydrogen Balmer lines, they do not have extended wings. We can roughly distinguish two types of Fe II line emission profiles: a) fairly symmetrical (e.g. HD 45725, HD 48917); b) asymmetrical, where one of the peaks is either more intense or wider (e.g. HD 50013). In a given object, most Fe II line emission profiles have a similar shape. There are, however, few objects where the central depression in the line profiles, or the relative intensity of peaks, change from one line to another, even if they have been observed simultaneously (HD 45725, HD 120991, HD 148184). This may suggest the presence of some inhomogeneity in the CE. Most objects show similar Fe II line profiles from one observing date to another. Fe II line emission profiles show similarities in their global shape i.e., central depression and relative intensity of the emission peaks to those of Hβ and Hγ lines. Only in the extreme cases of pronounced asymmetries in Fe II lines do they also appear in Hα.

[1] IRAF is distributed by the National Optical Astronomy Observatories, which is operated by the Association of Universities for Research in Astronomy (AURA), Inc., under cooperative agreement with the National Science Foundation.

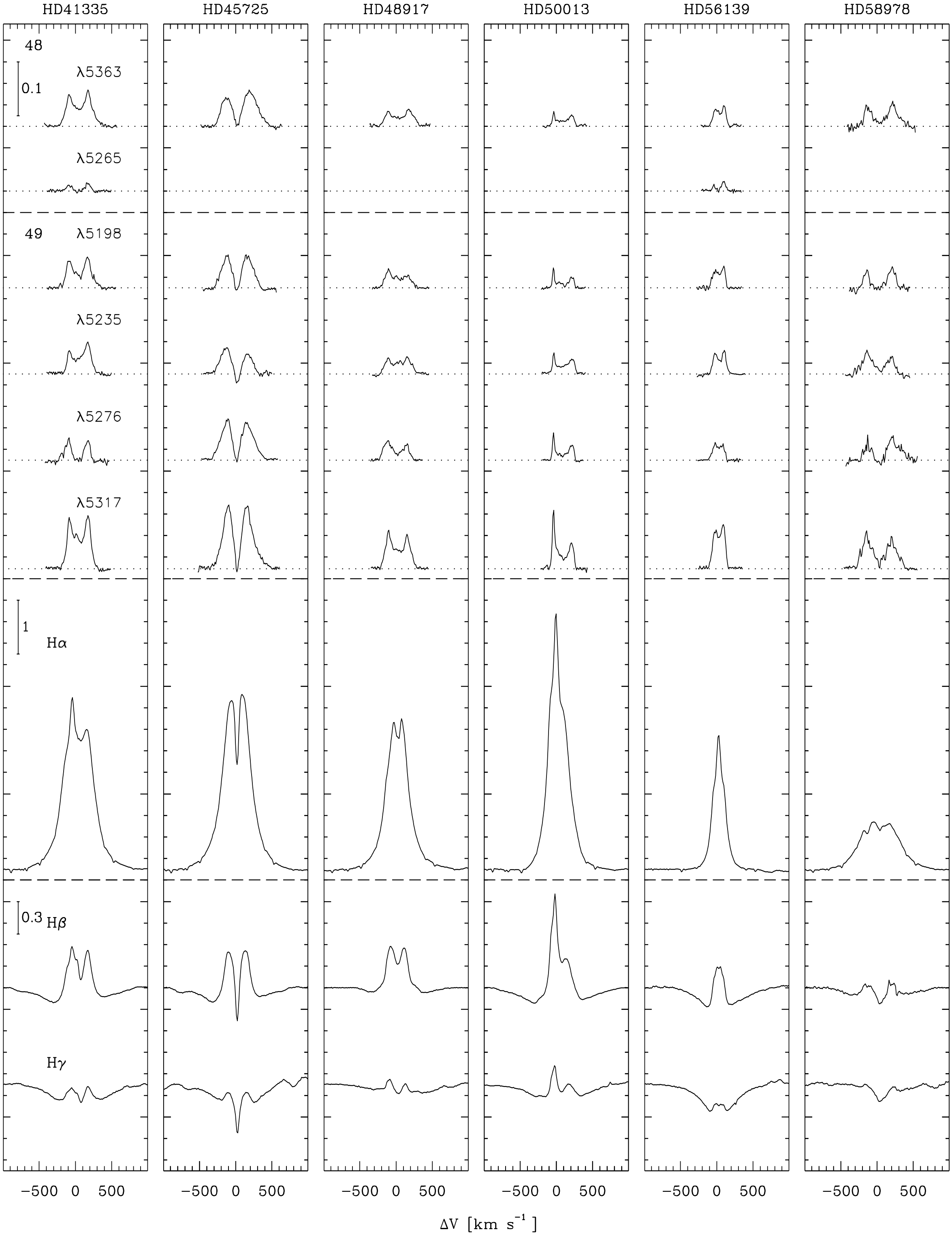

Fig. 1. Fe II and Balmer emission line profiles of some observed Be stars. The numbers in the upper corners of the left vertical panel of Fe II line profiles indicate the multiplet number to which the series of lines just below belong. The Fe II emission line profiles have all the same intensity scale, and Hβ and Hγ lines have a common intensity scale, which is different for Hα. Velocities in abscissas are heliocentric. See also the online catalogue of line profiles observed in other program stars.

4. Measurements and correlations

We performed the following measurements on each emission line profile: 1) central wavelength of lines, 2) intensity and velocity of the peaks and of the central depression, 3) line emission equivalent width (W), 4) separation of emission peaks (Δ_p), 4) widths at half intensity ($\Delta_{1/2}$) and at intensity $I/I_c = 1.0$ (Δ_1). As is known, some Fe II lines appear in the wings of stronger lines; for example, Fe IIλ4351 or Fe II of multiplet 42 are in the wings of Hγ and He I lines, respectively. We measured those lines only if the underlying line wings were well-defined. All these measurements are available in the online Table 5.

Figure 2 shows the equivalent widths W of all Fe II lines as a function of the emission-peak separation Δ_p in km s^{-1}, measured in four of the observed objects. The relation shown in Fig. 2 is representative of the behavior of W against Δ_p as seen in almost all studied objects; i.e. whatever the line strength of the Fe II line emissions in a given star, Δ_p, is the same within an average dispersion ±50 km s^{-1}. The same relation is also valid for line widths $\Delta_{1/2}$ and Δ_1, although in the last case, points are somewhat more scattered due to the measurement difficulties/uncertainties related to Δ_1. All W vs. Δ_p diagrams obtained are shown in the online Fig. 16.

If all Fe II lines were optically thin, this result would mean that there is a kinematically delimited formation region shared in the CE by all these lines. The average $\langle\Delta_p\rangle$ value can then be used as the typical Fe II-line emission-peak separation, in particular, when this quantity needs to be studied as a function of another stellar property, like rotation. Figure 3 shows $\langle\Delta_p\rangle$ versus $V \sin i$ of program objects. In the same figure we also plot $\langle\Delta_{1/2}\rangle$ and $\langle\Delta_1\rangle$ as a function of $V \sin i$. The correlations obtained agree with results in previous works, although in most cases authors used a reduced number of individual Fe II lines from different multiplets (Hanuschik 1987, 1988; Ballereau et al. 1995; Slettebak et al. 1992). The dashed line in each box of Fig. 3 is the linear regression fit for which the slopes and correlation coefficients are:

$$\left.\begin{array}{lll} \overline{\Delta_p} & = 0.86 \times V \sin i + \ \ 21; & r = 0.82 \\ \overline{\Delta_{1/2}} & = 1.10 \times V \sin i + \ \ 85; & r = 0.85 \\ \overline{\Delta_1} & = 1.25 \times V \sin i + 147; & r = 0.87 \end{array}\right\}. \quad (1)$$

Due to uncertainties in determining the widths of individual lines, small differences may exist in the regression line coefficients obtained in previous works, because in the present estimation they correspond to the average widths obtained from many individual lines. In our case, the uncertainties of slopes are ≈±0.20 on average. All these results can then be considered consistent. Since the slopes derived from average widths coincide with those of individual lines, it can be concluded that all Fe II lines share the same delimited formation region.

The dotted line added to correlations in Fig. 3 corresponds to $\Delta = 2V \sin i$. This line gives an upper limit to the expected rotational broadening of line profiles. Values $\langle\Delta_1\rangle \gtrsim 2V \sin i$ would imply that line-broadening mechanisms other than rotation can be operating. A tight relation $\langle\Delta_1\rangle = 2V \sin i$ would mean coupling or co-rotation of the inner CE layers with the star. The co-rotation could be produced by magnetic fields whose presence might be suspected (Neiner et al. 2003; Neiner 2006).

All measurements carried out on Balmer emission lines were performed on profiles corrected for the underlying photospheric absorption component following the procedure applied by Chauville et al. (2001). These measurements are given in the online Table 6. As in previous works (cf. Andrillat & Fehrenbach 1982; Dachs et al. 1986; Slettebak et al. 1992), the widths of Balmer lines correlate with $V \sin i$, except the width at intensity $I/I_c = 1.0$, which is not only more difficult to measure but can also be affected by several different broadening mechanisms, in particular, the electron scattering (Castor et al. 1970). We found, however, that, to our knowledge, it has not yet been shown so clearly in other previous attempts. We see that the equivalent width of the central depression, W_{cd}, of Hβ, Hγ, and Hδ emission lines show quite a well-defined trend defined with $V \sin i$ (average regression coefficients $r \simeq 80\%$). This result is shown in Fig. 4. It appears then that the CE region producing the emission and the central top-absorption depression in the Hβ, Hγ, and

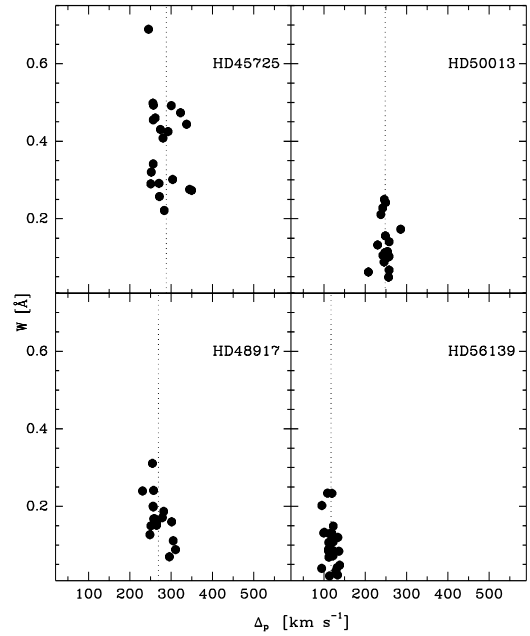

Fig. 2. Equivalent widths W (Å) of individual Fe II emission lines against their peak separation Δ_p (km s^{-1}) in four observed Be stars. All Δ_p are nearly the same for a given star, which suggests a common formation region. Vertical dotted lines indicate the average values of Δ_p. See also the online Fig. 16.

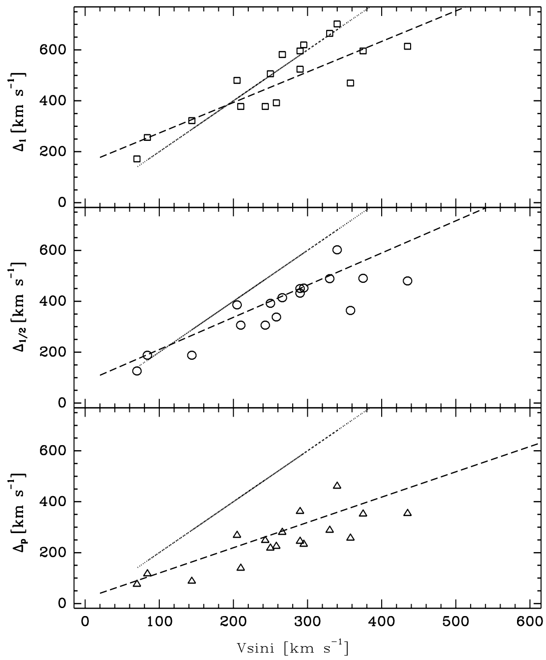

Fig. 3. Average widths of Fe II emission lines per star against the corresponding $V \sin i$. *From top to bottom*: $\langle\Delta_1\rangle$ = width at intensity $I/I_c = 1.0$, $\langle\Delta_{1/2}\rangle$ = width at half intensity, $\langle\Delta_p\rangle$ = separation of peaks. The dotted line in each block represents $\Delta = 2V \sin i$. The dashed lines are the regressions given in (1).

Hδ lines is somewhat flattened. On the other hand, we note that the average inclination angle of the rotational axis of program Be stars is low, $\langle i\rangle = 48° \pm 21$ (see Table 1). Since the mentioned self absorptions in the Balmer line emission profiles do not have negligible equivalent widths, $W_{cd} \lesssim 0.3$ Å, discs must have non negligible optical depth in the perpendicular direction to the equator.

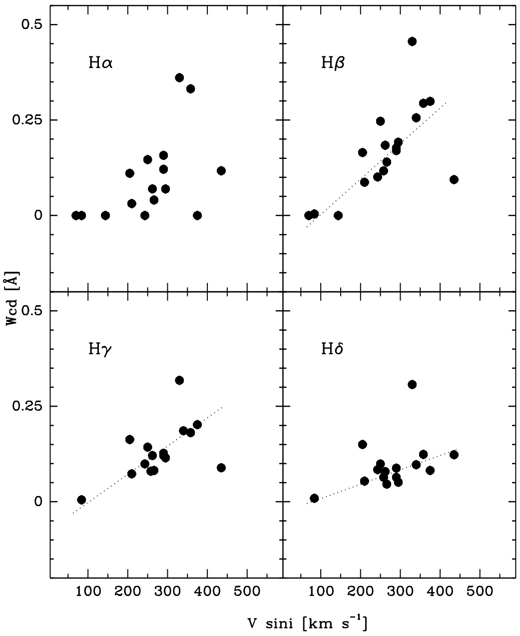

Fig. 4. Equivalent width of the central depression in Balmer emission lines $W_{\rm cd}$ against the $V \sin i$. The dotted lines are only indicative of the observed trends. These trends suggest that the Balmer emission line formation region is somewhat flattened.

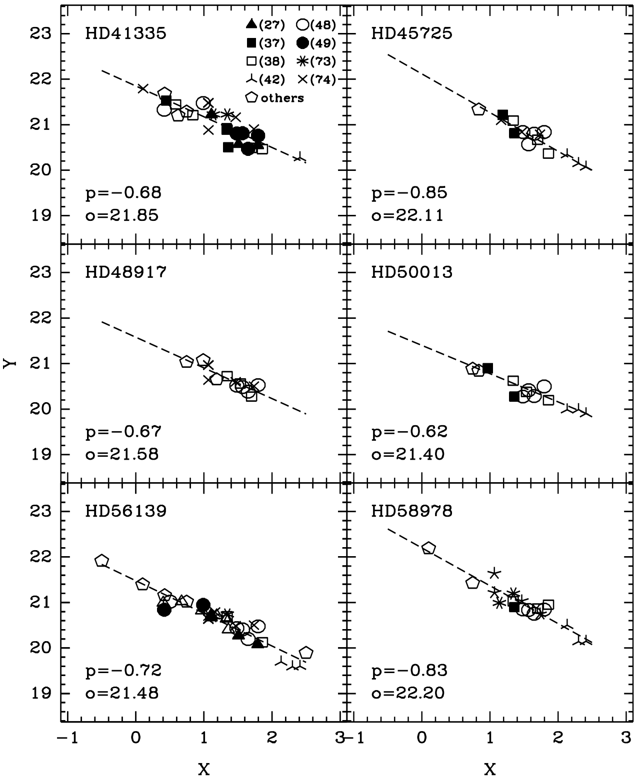

Fig. 5. Empirical SAC slopes for some stars whose lines are shown in Fig. 1. Each symbol corresponds to a given multiplet. The correspondence between symbols and multiplets is shown in the first left upper panel. In each panel are also given the slope $p = \partial Y/\partial X$ and o = ordinate at $X = 0$. The slopes indicate that Fe II lines are optically thick. Optically thin lines would produce slopes $p \approx 0$. See also the SAC of all program stars in the online Fig. 17.

5. The SAC method

To analyze emission lines, Wellman (1952) and Viotti (1970) developed empirical methods similar to "curves-of-growth". Friedjung & Malakpur (1971) proposed a different formalism that later became the self-absorption-curve method (SAC, Muratorio 1985; Friedjung & Muratorio 1987). While the curve-of-growth methods reveal effects related to the atomic level population in the emitting layers, the SAC method makes the opacity effect explicit on the emitted radiation intensity. It then carries information on the optical depth regime that controls the Fe II line emission formation in the CE of Be stars. The SAC method has been successfully applied to studying CE in a number of different types of objects: luminous blue stars (Muratorio & Friedjung 1988, Muratorio et al. 1992), B[e] stars (Muratorio et al. 2002a), P Cygni (Muratorio et al. 2002b), novae (Selvelli & Friedjung 2003), symbiotic stars (Kotnik-Karuza et al. 2002), the Be star component in Z CMa (van den Ancker 2004), etc. In this paper, we use the SAC method to determine the optical depth regime of Fe II emission lines observed in 17 Be classical stars and to estimate the extent of their formation region in the CE (HD 164284 has Fe II lines too small to be measured reliably).

The SAC method assumes that the emitting region is a flat disk with uniform density and temperature, which is characterized by the optical depth $\tau_{\rm o}$ in the center of a given spectral line. By comparing the *empirical* SAC with the *theoretical* one, we can derive the sought physical quantities. The theoretical SAC is defined by the relation $Y_\lambda = Y_\lambda(X_\lambda)$ where the respective variables (X_λ, Y_λ) are defined as follows (Friedjung & Muratorio 1987):

$$\left.\begin{aligned} X_\lambda &= \log \tau_l - \log (N_l/g_l) - C_1 \\ Y_\lambda &= Q(\tau_l) + \log (N_u/g_u) + C_2 \end{aligned}\right\}, \qquad (2)$$

where τ_l is the opacity in the central wavelength of the spectral line; $N_{u,l}$ and $g_{u,l}$ are the populations and statistical weights of the corresponding upper and lower atomic levels, respectively; $Q(\tau_l)$ is the theoretical SAC curve that measures the emitting efficiency of the studied environment and thus, it describes the self absorption in the spectral line; and C_1 contains atomic parameters, while C_2 depends on the area of the emitting region and on its characteristic velocity. The simplest form of the theoretical SAC function $Q(\tau_l)$ is:

$$Q(\tau_l) = \log\,[(1 - {\rm e}^{-\tau_l})/\tau_l]. \qquad (3)$$

From (2) and (3) it follows that for optically thin lines ($\tau_l \ll 1$) $Q(\tau_l) \simeq 0$, so that the corresponding SAC curves are horizontal lines ($\partial Y/\partial X = 0$). In contrast, optically thick lines ($\tau_l \ll 1$) produce a nearly straight slope. In the limit $\tau_l \gg 1$ the slope of the SAC curve is $\partial Q/\partial \log \tau_l \rightarrow -1$. Since on average velocity rates in the CE are larger than the thermal velocity, to derive (3) it was assumed that the intrinsic line profile is rectangular. The use of more realistic atomic line profiles complicates considerably the aspect of $Q(\tau_l)$. However, it does not change its formal dependence on the opacity significantly (Friedjung & Muratorio 1987). In this work we use relation (3). Some uncertainties related to this approximation are discussed in Sect. 7.

The empirical counterpart of (2) is given by:

$$\left.\begin{aligned} X_\lambda &= \log (g_l f_{ul} \lambda_{\rm o}) \\ Y_\lambda &= \log (F_{ul} \lambda_{\rm o}^3 / g_l f_{ul}) \end{aligned}\right\}, \qquad (4)$$

where F_{ul} is the integrated flux in a given line, f_{lu} is the oscillator strength of the transition, and $\lambda_{\rm o}$ the central wavelength of the line. The empirical SAC is constructed with individual (X_λ, Y_λ) multiplet segments, assuming that all multiplets have the same function $Q(\tau_l)$, i.e. the same formation region. Horizontal displacements of SAC segments of those multiplets with a common lower level with respect to a chosen reference multiplet, as well as vertical displacements of multiplet segments with common upper levels, lead to an estimate of relative level populations and of the average line excitation temperature. Comparison of the recomposed empirical SAC with the theoretical curve $Q(\tau_l)$ gives the optical depth of the reference-line multiplet and the radius of the corresponding emitting region.

6. Results

The equivalent widths of the Fe II lines studied in this work are given in the online Table 5. The corresponding atomic data are in the online Table 7. The continuum fluxes at the respective line frequencies as a function of the stellar fundamental parameters given in Table 1 are from the Kurucz (1992) LTE models atmospheres. As an example of SAC curves obtained, Fig. 5 shows those of objects referred to in Fig. 1. The whole set of SAC curves obtained in this work are shown in the online Fig. 17. The (X_λ, Y_λ) slopes of all program stars were fitted with straight lines. Figure 5 also gives the respective values of slopes (p) and y-intercept ordinates (o). The slopes obtained for all program stars range as:

$$-0.5 \pm 0.1 \lesssim \partial Y_\lambda/\partial X_\lambda \lesssim -1.0 \pm 0.1. \quad (5)$$

According to the discussion in Sect. 5, (5) clearly shows that *the studied Fe II emission lines are optically thick*. The individual values of $\partial Y/\partial X$ are listed in Table 2. As no studied line is optically thin, the horizontal part of the SAC curves in Figs. 5 and 17 is missing.

Since we cannot determine the location of the flat part of the SAC, the matching of the empirical SAC with $Q(\tau_l)$ is not obvious. To evaluate the optical depth τ_o of the reference Fe II line multiplet, we thus preferred to equate the empirical slopes obtained using (4) with the theoretical slope derived from (3):

$$\left(\partial Y_\lambda/\partial X_\lambda\right)_{\rm empirical} = \partial Q(\tau)/\partial \log\tau. \quad (6)$$

Assuming that the atomic level populations do not depart from Boltzmann statistics, although the population can deviate from LTE conditions, the relative displacements of the SAC segments of different multiplets with a common upper or lower level can be written as: $|\Delta(X,Y)| = (\chi_1-\chi_2)5040/T_{\rm ex}$, where χ_1 and χ_2 are the excitation potentials of two given levels and $T_{\rm ex}$ is the corresponding excitation temperature. However, when the excitation temperature is high, as in program stars, these displacements are small and the determination of $T_{\rm ex}$ is difficult. We then preferred to determine $T_{\rm ex}$ by using an alternative iteration process. To this purpose, we defined the following variables U and V:

$$\left.\begin{array}{rcl} U &=& X_\lambda + Y_\lambda - \log(1-{\rm e}^{-\tau}) \\ V &=& \chi - \chi_{\rm o} \\ \tau &=& \tau_{\rm o}10^{\frac{5040}{T_{\rm ex}}(\chi-\chi_{\rm o})}10^{(X_\lambda - X_{\rm o})} \end{array}\right\}, \quad (7)$$

which determine a straight line $U = U(V)$ whose slope, controlled with the χ^2 test, is $5040/T_{\rm ex}$. According to the star, we used as reference multiplet the one with the average wavelength lieing roughly in the middle of the re-composed SAC (frequently multiplet 38). Finally, to estimate the emitting region extent, we used the explicit form of the SAC obtained from relations (2) and (4) (Friedjung & Muratorio (1987):

$$\mathcal{S} = \frac{1}{2\pi hc}\left[\frac{10^{-Q(\tau_{\rm o})}}{\tau_{\rm o}}\right]\frac{F_{\rm c}\,W_\lambda\,\lambda^4}{V_{\rm o}}\,{\rm e}^{1.44/\lambda T_{\rm ex}} \quad (8)$$

Table 2. Parameters of the Fe II line emission formation derived from the SAC curves.

Object	$\partial Y/\partial X$ SAC	$\tau_{\rm o}$	$T_{\rm ex}$ K	$V_{\rm o}$ km s^{-1}	$R_{\rm e}/R_*$ SAC	$R_{\rm H}/R_*$ $j=1$	$R_{\rm H}/R_*$ $j=0.5$
HD 41335	–0.68	2.0	7600	182	2.0	2.8	7.8
HD 45725	–0.85	3.1	4500	245	4.2	2.3	5.3
HD 48917	–0.67	2.0	5000	193	2.3	1.5	2.3
HD 50013	–0.62	1.7	8800	153	1.1	2.0	3.8
HD 56139	–0.72	2.2	7000	94	1.7	1.4	2.1
HD 58978	–0.83	2.9	11 600	245	1.3	2.1	4.5
HD 63462	–0.94	4.3	13 300	247	*	2.5	6.0
HD 88661	–0.95	4.5	6000	216	1.5	1.6	2.6
HD 91465	–0.73	2.2	5500	207	2.8	2.0	3.8
HD 105435	–0.49	1.2	5900	169	2.2	2.3	5.3
HD 110335	–0.65	1.8	5400	196	1.9	2.3	5.3
HD 112091	–0.72	2.2	7100	153	1.1	3.0	9.0
HD 120991	–0.65	1.8	6500	63	1.8	1.8	3.4
HD 124367	–0.83	2.9	5300	226	3.0	2.5	6.4
HD 148184	–0.69	2.0	12 000	94	1.1	3.3	10.7
HD 157042	–0.65	1.8	6900	301	1.7	1.5	2.2
HD 158427	–0.61	1.7	6000	225	1.5	2.4	5.6

$\tau_{\rm o}$ = average optical depth of Fe II lines in multiplet 38; $T_{\rm ex}$ = average excitation temperature of Fe II lines; $V_{\rm o}$ = characteristic emission line width in velocity units; $R_{\rm e}/R_*$ = radius of the Fe II line formation region derived with the SAC; $R_{\rm H}/R_*$ = radius derived with Huang's (1972) relation for optically thin lines.
*: $R_{\rm e}/R_* \approx (R/R_*)/\sqrt{\cos i}$ ($R/R_* \approx 1$, $i \sim 90^{\rm o}$).
Note: HD 164284 has too tiny Fe II emission lines to perform any reliable measurement.

where S is the surface of the emitting region, $V_{\rm o}$ is a characteristic emission line width in velocity units, $F_{\rm c}$ the flux of the continuum spectrum at the given line wavelength, and W_λ the line equivalent width. Using $\tau_{\rm o}$ issued from (6) and $T_{\rm ex}$ iterated in (7), from relation (8), we obtain $\mathcal{S} = \pi(R_{\rm e}^2 - R_*^2)$. However, as the "observed" emitting surface is aspect-angle-dependent, to calculate the radius $R_{\rm e}/R_*$ of the line emission formation region, we have corrected the area derived from (8) using $\mathcal{S} \to \mathcal{S}\cos i$. The inclination angle i used in this correction is given in Table 1. We note that since the effect of i on the estimate of $R_{\rm e}/R_*$ is proportional to $1/\sqrt{\cos i}$, the uncertainties on i do not introduce sensitive changes in $R_{\rm e}/R_*$. In (8) it is implicitly assumed that ${\rm e}^{1.44/\lambda T_{\rm ex}} \gg 1$. However, we do not obtain qualitatively different results for $\tau_{\rm o}$ and $R_{\rm e}/R_*$ when dropping this approximation. All quantities describing the Fe II emission region obtained in the present section are given in Table 2. For comparison, in this table the radii of the Fe II region calculated from Huang's (1972) expression are also given: $R_{\rm H}/R_* = (2V\sin i/\Delta_{\rm p})^{1/j}$ ($j = 1/2$ for Keplerian rotation; $j = 1$ for rotation with conservation of angular momentum), which actually should be used only for optically thin lines.

7. Discussion

In this section we briefly discuss three different, but related issues: the incidence of the line opacity regime on the estimate of the extent of the line-formation zone, formulation of the SAC by taking into account the optical depth in the line source function, and the interpretation of the line excitation temperature, which in the SAC method does not straightforwardly relate to the physical properties of the line-formation region.

7.1. Opacity of the Fe II line emission formation region

One of the main results in this work is that the Fe II emission lines in the CE of the studied classical Be stars are optically thick. This means that models of Fe II line emission formation in Be stars, which can help to diagnose the physical properties of CE more precisely, must take the optical depth effects in these lines into account. The values of optical depths obtained are on average $\langle\tau_o\rangle = 2.4 \pm 0.9$. Even though uncertainties may be affecting the estimate of individual τ_o values, the empirical SAC curves of Fig. 5 and those given in the online Fig. 17, show that slopes are far from being horizontal lines, which would be the case if Fe II lines were optically thin. The temperature structure of the CE in γ Cas and 1 Del between 1 and 2 stellar radii derived by Jones et al. (2004) is also consistent with optically thick Fe II lines, which could otherwise act as an efficient cooling agent.

The extent of the Fe II emission-line formation region we obtained is on average $\langle R_e/R_*\rangle = 2.0 \pm 0.8$. It is then systematically smaller than the one obtained from Huang's (1972) relation with $j = 0.5$: $\langle R_H/R_*\rangle_{j=0.5} = 5.1 \pm 2.4$, valid only for optically thin lines. From (8), where $R_e/R_* \sim (1 - e^{-\tau_o})^{-1}$, we can see that the smaller is τ_o the larger R_e/R_* becomes, in accordance with Huang's estimates that are valid for $\tau_o \to 0$. Relation (8) can be reformulated for optically thin lines by considering that in this case $W_\lambda \sim \sqrt{\pi}\tau_o\Delta\lambda_D$, where $\Delta\lambda_D$ = thermal Doppler line width. For some stars the SAC radii given in Table 2 are of the same order of magnitude as those obtained form Huang's (1972) formula. This is probably due to the uncertainties related to the T_{ex} determination.

In the present discussion we compare radii issued from two different formulations. On the one hand, there is relation (8) that ignores details on the kinematical properties of regions where the lines are formed. On the other, there is Huang's (1972) relation, which is based only on the kinematical aspects of the CE. However, several contributions have shown that the separation of emission peaks is a function of the velocity fields and the CE optical depth. Cidale & Ringuelet (1989) found that in static CE the separation of the emission peaks is wider when the value of the optical depth τ_o is higher. On the contrary, in moving, optically thick CE the interplay of opacity and velocity fields can lead to a reduction of the emission peak separation as τ_o increases (Hummel 1994; Arias 2004; Arias et al. 2004, 2006).

7.2. The line source function and the SAC

In circumstellar layers where the Fe II line emissions are formed, $R \lesssim 2R_*$, the temperature can be estimated assuming that the only energy input is from the geometrically diluted stellar radiation filed. Moujtahid et al. (2000) show that this approximation is valid for a CE close to the star:

$$T_{CE} \approx W(R)^{1/4} T_{eff} \quad (9)$$

where $W(R)$ is the geometrical dilution factor. In radii $R \lesssim 2R_*$, T_{CE} is nearly the same as the thin disc temperature T_D derived using more detailed models (Carciofi & Bjorkman 2006). Although the distances of the Fe II emission line regions derived in the present work are short, the excitation temperatures T_{ex} are on average 30% smaller than T_{CE} given by (9). This reveals that non-LTE effects control the population of atomic levels in the line transitions. The level-populations are currently written as $N_{u,l} = b_{u,l}N^*_{u,l}$ (sub-indices "u, l" stand for "upper" and "lower" level), $b_{u,l}$ are the respective non-LTE deviation coefficients and $N^*_{u,l}$ are the level populations in LTE. By definition it

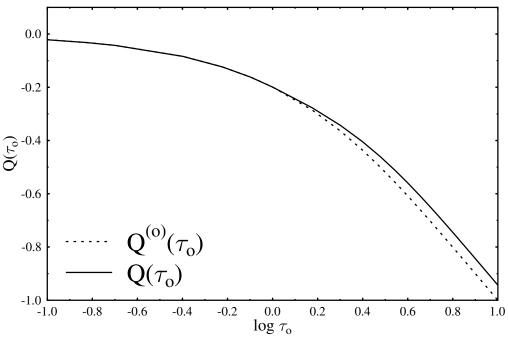

Fig. 6. Comparison of the SAC curve $Q(\tau_o)$ given by (12) with $Q^{(o)}(\tau_o)$ calculated in (3).

is $\Delta\chi/T_{ex} = \Delta\chi/T_{CE} - \ln(b_u/b_l)$, where $\Delta\chi = \chi_u - \chi_l$ is the difference of excitation potentials. We would then expect roughly that $b_u/b_l \sim e^{-0.6\Delta\chi/T_{CE}}$, which implies that $b_u \neq b_l$. This also means that the source function S_λ of each line is decoupled from the local Planck function $B_\lambda(T_{CE})$. As in this case there must be non-local feeding of energy, the source function becomes dependent on the line optical depth (Mihalas 1978, Chap. 11). The line source function $S_\lambda(\tau_o)$ can then be approximately written as (Cidale & Ringuelet 1989):

$$S_\lambda(t_o) = \begin{cases} S_o & \text{for } t_o \lesssim 1 \\ S_o \times t_o^q & \text{for } t_o > 1, \end{cases} \quad (10)$$

where the factor S_o depends on the nature of the source function (see next section) and q depends on whether the intrinsic line-absorption profile is of Lorentz type, or Gaussian: $0.28 \lesssim q \lesssim 0.6$. To derive the SAC function $Q(\tau_o)$ that reflects the opacity dependence of the source function given in (10), we write the flux per unit wavelength produced by a CE of total optical depth τ_o as:

$$F_o = \mathcal{S}\int_0^{\tau_o} S_o(t_o)e^{-t_o}dt_o \quad (11)$$

where $\mathcal{S}$ is the area of the emitting surface projected in the observer's direction. Considering $S_o = B_o(T_{ex})$ = constant, the integration of (11) leads to the function $Q(\tau_o)$ given by (3) (Friedjung & Muratorio 1987) and used in the present work. T_{ex} is the excitation temperature of the Fe II lines, which is assumed to be the same for all studied lines. However, adopting $S_o = B_\lambda(T_{ex})$ as before, but considering the opacity-dependence of the source function indicated in (10), from (11) we obtain:

$$10^{Q(\tau_o)} = \begin{cases} (1 - e^{-\tau_o})/\tau_o & \text{for } \tau_o \lesssim 1 \\ \left[(1 - e^{-\tau_o}) + \int_1^{\tau_o}(t^q - 1)e^{-t}dt\right]/\tau_o & \text{for } \tau_o > 1. \end{cases} \quad (12)$$

In Fig. 6 the SAC function $Q(\tau_o)$ defined in (12) is compared with $Q^{(o)}(\tau_o)$ given by (3). $Q(\tau_o)$ has similar properties as $Q^{(o)}(\tau_o)$, i.e. $Q(\tau_o \ll 1) \to 0$ and $\partial Q/\partial \ln\tau \to -1$ for $\tau_o \gg 1$. However, for $\tau_o \gtrsim 1$ a given slope $\partial Q(\tau_o^{new})/\partial\log\tau = \partial Q^{(o)}(\tau_o^{old})/\partial\log\tau$ implies $\tau_o^{new} > \tau_o^{old}$, as is shown in the following table, where the slopes due to "old" opacities are reinterpreted with the "new" SAC curve:

	τ_o									
"old"	1.0	2.0	3.0	4.0	5.0	6.0	7.0	8.0	9.0	10.0
"new"	1.3	2.6	3.8	4.9	6.0	7.0	8.1	9.1	10.2	11.0

7.3. The CE line-emitting power

In the present formulation of the SAC, all information on the nature of the Fe II-line source function and on its relation to the physical properties of the line formation region is hidden in the $T_{\rm ex}$ parameter. To inquire in what way the SAC method can be improved to draw some information from $T_{\rm ex}$, let us write the line source function S_λ in the two level-atom approximation (Thomas 1965, 1983; Mihalas 1978):

$$S_\lambda = \left[\int_0^\infty \phi_\lambda J_\lambda {\rm d}\lambda + \epsilon B_\lambda(T_{\rm CE}) + \eta B_\lambda(T_r)]/[1+\epsilon+\eta\right] \quad (13)$$

where ϕ_λ is the intrinsic line absorption profile; J_λ is the angle-averaged intensity of the radiation field; ϵ depends on the upper level collision-depopulating rates; η represents the depopulation rate of the upper level by photoionization processes; $B_\lambda(T_{\rm CE})$ is the Planck function for the local electronic temperature $T_{\rm e} = T_{\rm CE}$; T_r is a "radiation temperature", whose value is set by the photoinization and recombination rates. The source function can be collision-dominated if $\epsilon > \eta$ and $\epsilon B(T_{\rm CE}) > \eta B(T_r)$, radiation-dominated if $\epsilon < \eta$ and $\epsilon B(T_{\rm CE}) < \eta B(T_r)$, and mixed-dominated in other compararative combinations of these terms. According to the source function nature, the $S_{\rm o}$ factor in (10) becomes:

$$S_{\rm o} \approx \begin{cases} \epsilon^{1/2} B_\lambda(T_{\rm CE}) & \text{for collision−dominated} \\ \eta^{1/2} B_\lambda(T_r) & \text{for radiation−dominated.} \end{cases} \quad (14)$$

Thus, depending on the spectral line, local electron temperature, electron density, and the radiation field, $T_{\rm ex}$ reflects either the local electron temperature (collision-dominated), the stellar radiation field (radiation-dominated), or some combination of both (mixed-domination) that would be important to specify in further attempts of studying Fe II lines. By considering only the leading factors of the intervening radiative and collisional rates in ϵ, η, and $B(T_r)$, we can determine the nature of the source function and its incidence on the values of $T_{\rm ex}$. This can also help to appreciate the relation between the value of $T_{\rm ex}$ and the radius derived of the Fe II line-formation region. Let us then write

$$\left.\begin{array}{rcl} \epsilon & \simeq & C_{ul}/A_{ul} \\ \eta & \simeq & R_{uk}/A_{ul} \\ B(T_r) & \simeq & \frac{2h\nu_{ul}^3}{c^2}\left[{\rm e}^{h\nu_{ul}/kT_{\rm e}\frac{R_{uk}}{R_{lk}}\frac{R_{kl}}{R_{ku}}} - 1\right]^{-1} \end{array}\right\}, \quad (15)$$

where C_{ul} are the collisional rates, R_{nk} and R_{kn} are respectively the radiative ionization and recombination rates to the n-atomic level, and A_{ul} is the spontaneous emission rate. To calculate R_{nk}, we approximate the photoionization radiation field with $J_\nu = W(R)B_\nu(T_{\rm eff})$ (Vinicius et al. 2005). Table 6 gives the average source function parameters normalized to the local continuum flux $F_{\rm c}$. They were calculated using lines of multiplets 27, 38, 49, and the following parameters for typical Be stars (spectral type B1-B2): $T_{\rm eff}$ = 25000 K, electron density $N_{\rm e} = 3\times10^{12}$ cm^{-3}, electron temperature $T_{\rm CE}$ derived with (9).

Values in Table 6 show that the source function varies from genuine radiation-dominated at $R/R_* = 1.5$ to mixed-dominated in $R/R_* = 5.0$ [$\eta \sim \epsilon$ and $\eta^{1/2}B(T_r)/F_{\rm c} \sim \epsilon^{1/2}B(T_{\rm CE})/F_{\rm c}$]. The lower block of Table 7.3 shows the dependence of $T_{\rm ex}$ on distance R, which implies that $T_{\rm ex} < T_{\rm CE} \ll T_{\rm eff}$. Thus, whenever $T_{\rm ex}$ is low compared to $T_{\rm eff}$, as it is for values in Table 5, it does not mean that the formation region of Fe II emission lines lies far from the central star. Since the source function is radiation-dominated in regions of its maximum emission effectiveness, the effect of the electron temperature on the production of Fe II lines is marginal, as it acts through negligible collisional terms.

Table 3. Fe II line source function parameters.

R/R_*	ϵ	ϵ/η	$\epsilon^{1/2}B(T_{\rm CE})/F_{\rm c}$	$\eta^{1/2}B(T_r)/F_{\rm c}$
1.5	0.03 ± 0.01	0.07 ± 0.03	0.06 ± 0.01	0.26 ± 0.17
3.0	0.05 ± 0.02	0.35 ± 0.09	0.02 ± 0.01	0.06 ± 0.02
5.0	0.05 ± 0.02	0.81 ± 0.20	0.01 ± 0.00	0.01 ± 0.00
R/R_*		$T_{\rm CE}$ (K)	$S_{\rm o}/F_{\rm c}$	$T_{\rm ex}$ (K)
1.5		14 900	0.26 ± 0.14	$12\,400^{+2600}_{-3400}$
3.0		9800	0.06 ± 0.02	8210^{+650}_{-800}
5.0		7800	0.01 ± 0.00	5930^{+10}_{-40}

Finally, an explanation of the low values of radii R/R_* derived with the SAC is given by the rapid decrease with distance of $S_{\rm o} = \eta^{1/2}B(T_r)$, as seen in Table 6, which indicates that the Fe II emission-line formation zone in the CE cannot be very extended, or that it cannot be far from the central star. Short radii of the Fe II emission-line formation zone in Be stars $R_{\rm e} \sim 1.5\ R_*$ and low line-excitation temperatures ranging from 4500 to 6000 K have also been recently found by Brusasco & Cidale (2006, in preparation) using detailed non-LTE models.

8. Conclusions

We have performed an empirical analysis of the Fe II emission lines in Be stars to derive insights into the optical depth regime that characterizes these lines (optically thin or optically thick), as well as to obtain the average excitation temperature and the extent of their formation region in the CE.

We have presented observations of several series of Fe II line emission multiplets in the $\lambda\lambda$ 4230−7712 Å wavelength interval and the first three members of the hydrogen Balmer series, which were observed simultaneously in 18 southern Be stars. Although Fe II lines in Be stars have already been studied by several authors, most of them considered only the strongest lines in different multiplets. On the contrary, the present analysis is based on the use of a large number of Fe II line multiplets. Observations were carried out for enough Be stars to render the obtained statistical insights reliable.

The correlations between the Fe II emission-line widths and $V\sin i$ suggest that the line formation region in the circumstellar disc cannot be situated far from the central star. On the other hand, we found a rather well-defined correlation between the central depression in the Balmer emission lines with the $V\sin i$, which indicates that CE have globally flattened geometrical structures.

In the present paper we analyze only the Fe II emission lines in detail. In contrast to previous works on the Fe II lines in Be stars, where it is systematically assumed that they are optically thin, we have made allowance for their possibly optically-thick character. The Fe II emission lines were thus studied using the self-absorption-curve (SAC) method. This analysis leads us to conclude that *Fe II emission lines in Be stars are optically thick* and that the optical depth in the line center is on average $\tau_{\rm o}$ = 2.4 ± 0.9. It has also been obtained that *the line formation region lies on average near the central star, within R/R_* = 2.0 ± 0.8.*

Considering the collision- and radiation-dependent terms of the line source function, we confirm that due to its rapid decrease with the radius, the Fe II line-emission formation region cannot be neither extended nor located far from the star.

Due to the non-LTE effects, the optical-depth dependence of the Fe II line source function should be taken into account explicitly in further improvements to the SAC method. In general, to gain precision in the derived physical parameters, the empirical methods for studying Fe II emission lines need to consider: 1) the opacity regime of lines; 2) their absorption line profile; 3) the nature of the source function regarding the processes determining the excitation of atomic levels, 4) the velocity field in the formation region. This is the aim pursued in a forthcoming paper, where new series of observations of Fe II lines will complete the study.

Acknowledgements. We would like to thank Dr. J. Chauville for his help in the reduction of some of the data. We warmly thank the comments and suggestions formulated by the referee.

References

Allen, D. A., & Swings, J. P. 1976, A&A, 47, 293
Arias, M. L. 2004, Ph.D. Thesis, University of La Plata, Argentina
Arias, M. L., Zorec, J., & Ringuelet, A. 2004, BAAA, 47, 161
Arias, M. L., Zorec, J., Frémat, Y. 2006, In Active OB-Stars: laboratories for stellar and circumstellar physics, in press
Andrillat, Y., & Fehrenbach, Ch. 1982, A&AS, 48, 93
Ballereau, D., Chauville, J., & Zorec, J. 1995, A&ASS, 111, 457
Carciofi, A. C., & Bjorkman, J. E. 2006, ApJ, 639, 1081
Castor, L., Smith, L. F., & van Blerkom, D. 1970, ApJ, 159, 1119
Chauville, J., Zorec, J., Ballereau, D., et al. 2001, A&A 378, 861
Cidale, L. S., & Ringuelet, A. E. 1989, PASP, 101, 417
Collin-Souffrin, S., Joly, M., Heidmann, N., et al. 1979, A&A 72, 293
Collin-Souffrin, S., Joly, M., Heidmann, N., et al. 1980, A&A, 83, 190
Collins II, G. W. 1987, In IAU Coll., 92, 3
Dachs, J., Hanuschik, R. W., Kaiser, D., et al. 1986, A&A, 159, 276
Dachs, J., Hummel, W., & Hanuschik, R. W. 1992, A&ASS, 95, 437
de Geus, E. J., de Zeewv, P. T., & Lub, J. 1989, A&A, 216, 44
Divan, L., & Zorec, J. 1982, ESA-SP, 177, 101
Frémat, Y., Zorec, J., Hubert, A. M., et al. 2005, A&A, 440, 305
Friedjung, M., & Malakapur, I. 1971, Astrophys. Lett., 7, 171
Friedjung, M., & Muratorio, G. 1987, A&A, 188, 100
Geisel, S. L. 1970, ApJ, 161, 105
Hanuschik, R. W. 1987, A&A, 173, 299
Hanuschik, R. W. 1988, A&A, 190, 187
Huang, S. S. 1972, ApJ, 171, 549
Hubert-Delplace, A. M., & Hubert, H. 1979, An Atlas of Be Stars, Paris Meudon Observatory
Hummel, W. 1994, A&A, 289, 458
Jaschek, M., Slettebak, M., & Jaschek, C. 1981, Be Nwsl., 4, 9
Jones, C. E., Sigut, T. A. A., & Marlborough, J. M. 2004, MNRAS, 352, 841
Kotnik-Karuza, D., Friedjung, M., & Selvelli, P. L. 2002, A&A, 381, 507
Kurucz, R., 1992, Models of Stellar Atmospheres, CD Freeman & Co.
Mihalas, D. 1978, Stellar Atmospheres, 2nd. ed.,
Moujtahid, A., Zorec, J., & Hubert, A. M. 2000, in IAU Coll., 175, ASP Conf. Ser., 214, 506
Muratorio, G. 1985, Ph.D., Marsella University
Muratorio, G., & Friedjung, M. 1988, A&A, 190, 103
Muratorio, G., Viotti, R., Friedjung, M., et al. 1992, A&A, 258, 423
Muratorio, G., Friedjung, M., Rossi, C., et al. 2002a, Scientific Highlights SF2A 2002, p. 547
Muratorio, G., Markova, N., Friedjung, M., et al. 2002b, A&A, 390, 213
Neiner, C. 2006, in Active OB-Stars: Laboratories for Stellar and Circumstellar Physics, in press
Neiner, C., Hubert, A. M., & Frémat, Y., et al. 2003, A&A, 409, 275
Netzer, H. 1988, in Physics of Formation of Fe II Line Outside LTE, IAU Coll., 94, Ap&SS Lib. 138, 247
Polidan, R. S., & Peters, G. J. 1976, Be and Shell Stars, IAU Symp., 70, 59
Selvelli, P., & Friedjung, M. 2003, A&A, 401, 297
Slettebak, A. 1982, Be stars, IAU Symp., 98 (Dordrecht: D. Reidel Publishing Co.), 109
Slettebak, A., Collins II, G. W., & Truax, R. 1992, ApJ, 81, 335
Tarafdar, S. P., & Apparao, K. M. V. 1994, A&A, 290, 159
Thomas, R. N. 1965, Non-Equilibrium Thermodynamics in the Presence of a Radiation Field (Univ. Colorado Press)
Thomas, R. N. 1983, Stellar Atmospheric Structural Patterns, NASA SP-471, 76
Vinicius, M. M. F., Zorec, J., Leister, N. V., & Levenhagen, R. S. 2006, A&A, 446, 643
Viotti, R. 1970, Mem. Soc. Astron. Ital., 41, 513
Viotti, R. 1976, ApJ, 204, 293
Viotti, R., & Koubský, P. 1976, Be and Shell Stars, ed. A. Slettebak (Dordrecht, Holland; Boston: D. Reidel Pub. Co.), IAU Symp., 70, 99
van den Ancker, M. E., Blondel, P. F. C., Tjin A Djie, H. R. E., et al. 2004, MNRAS, 349, 1516
Wellmann, P. 1952, Z. Astrophys., 30, 71, 88, 96
Yudin, R.V. 2001, A&A, 368, 912
Zorec, J., Frémat, Y., & Cidale, L. 2005, A&A, 441, 235

Online Material

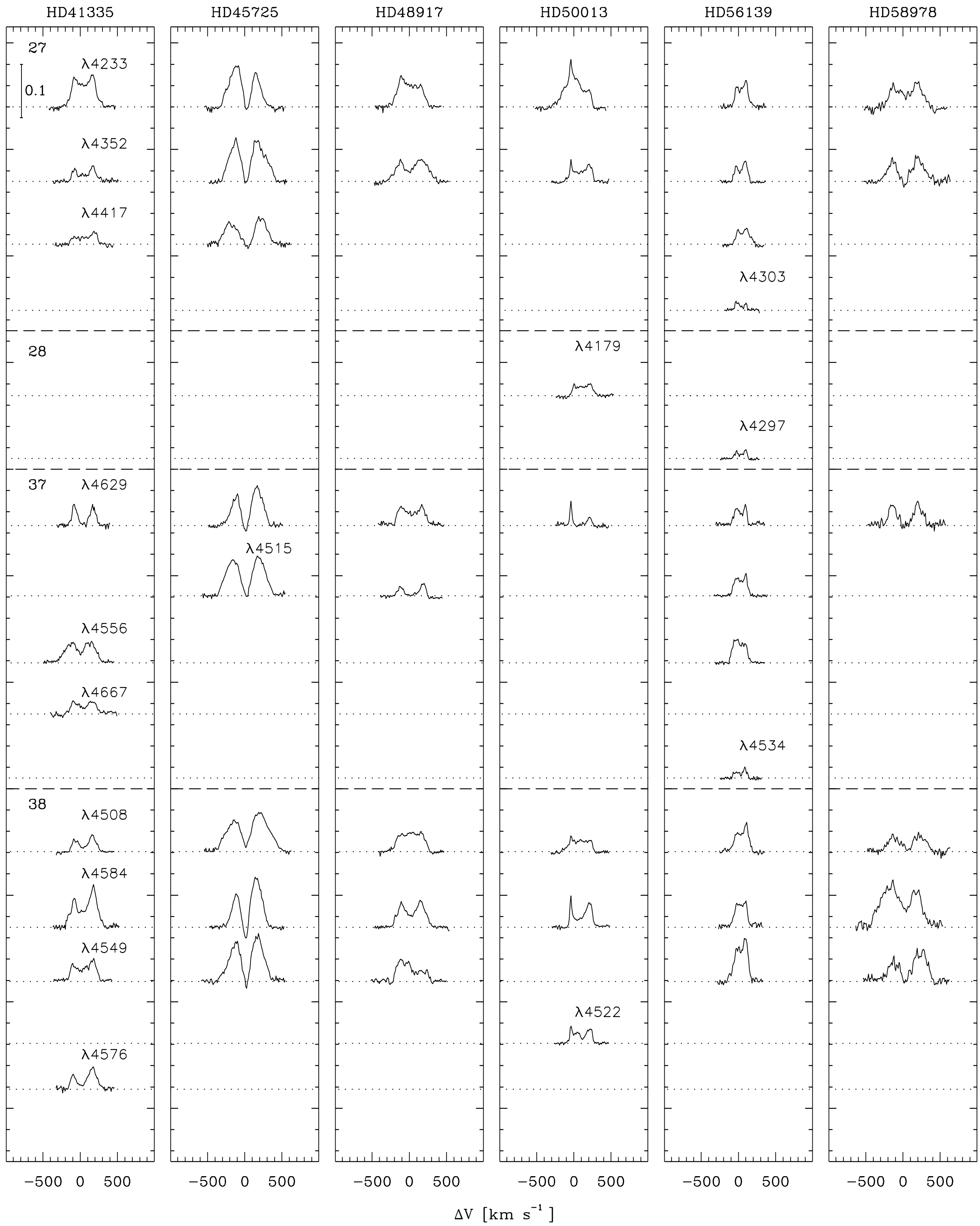

Fig. 7. Fe II and Balmer line-emission profiles of some observed Be stars. The number in the upper left hand corner of each column of Fe II line profiles indicates the line multiplet.

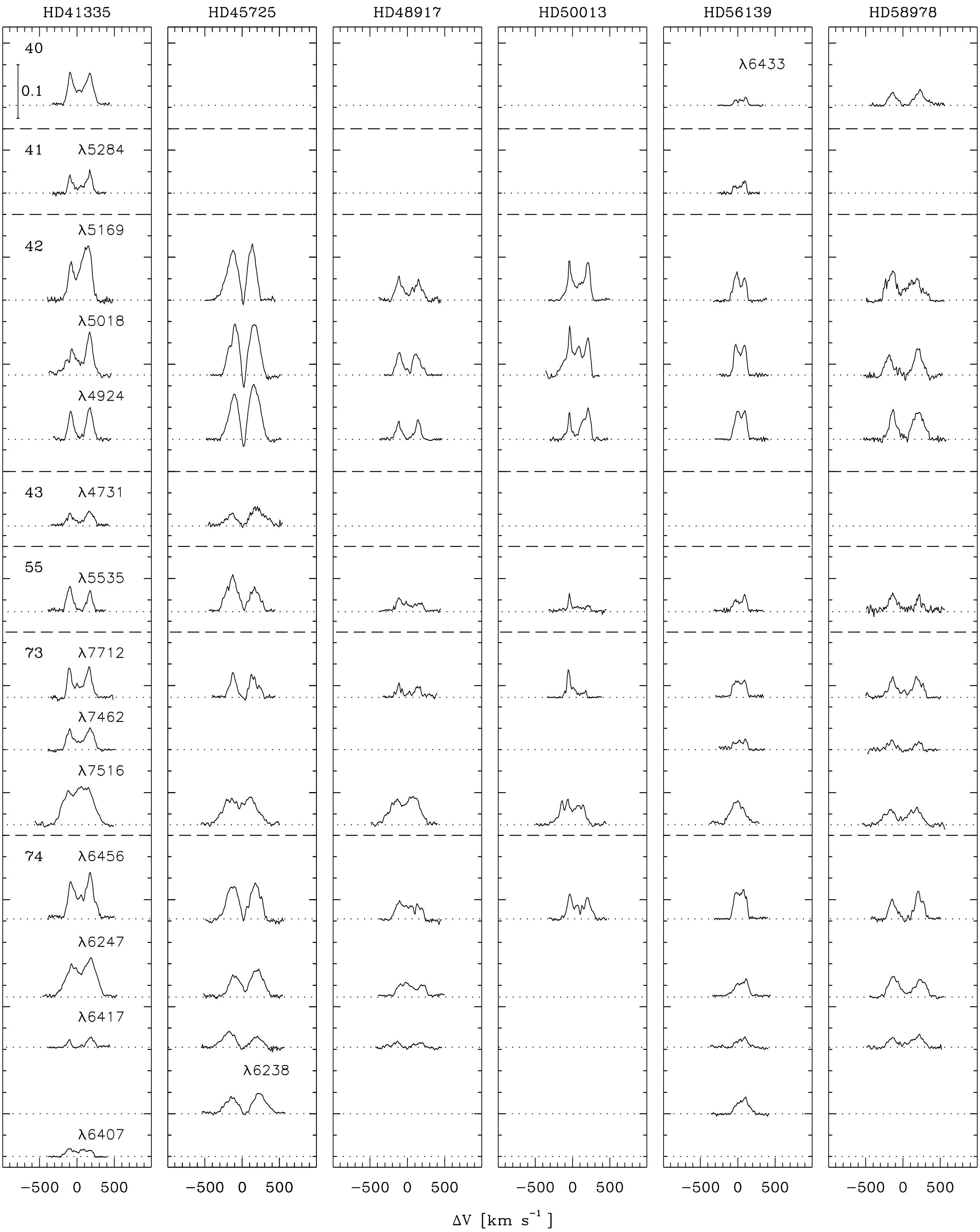

Fig. 8. Same as in Fig. 7.

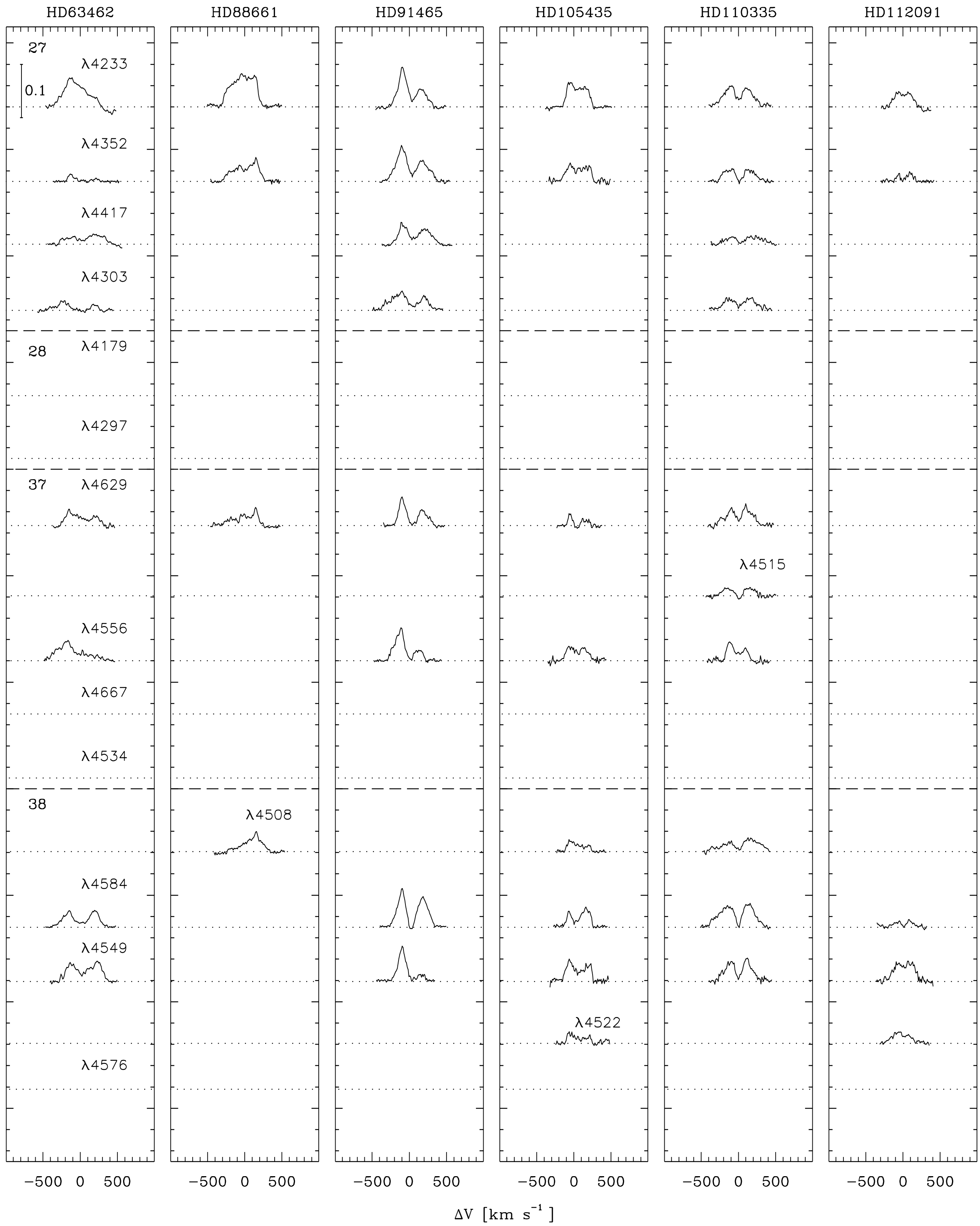

Fig. 9. Same as in Fig. 7.

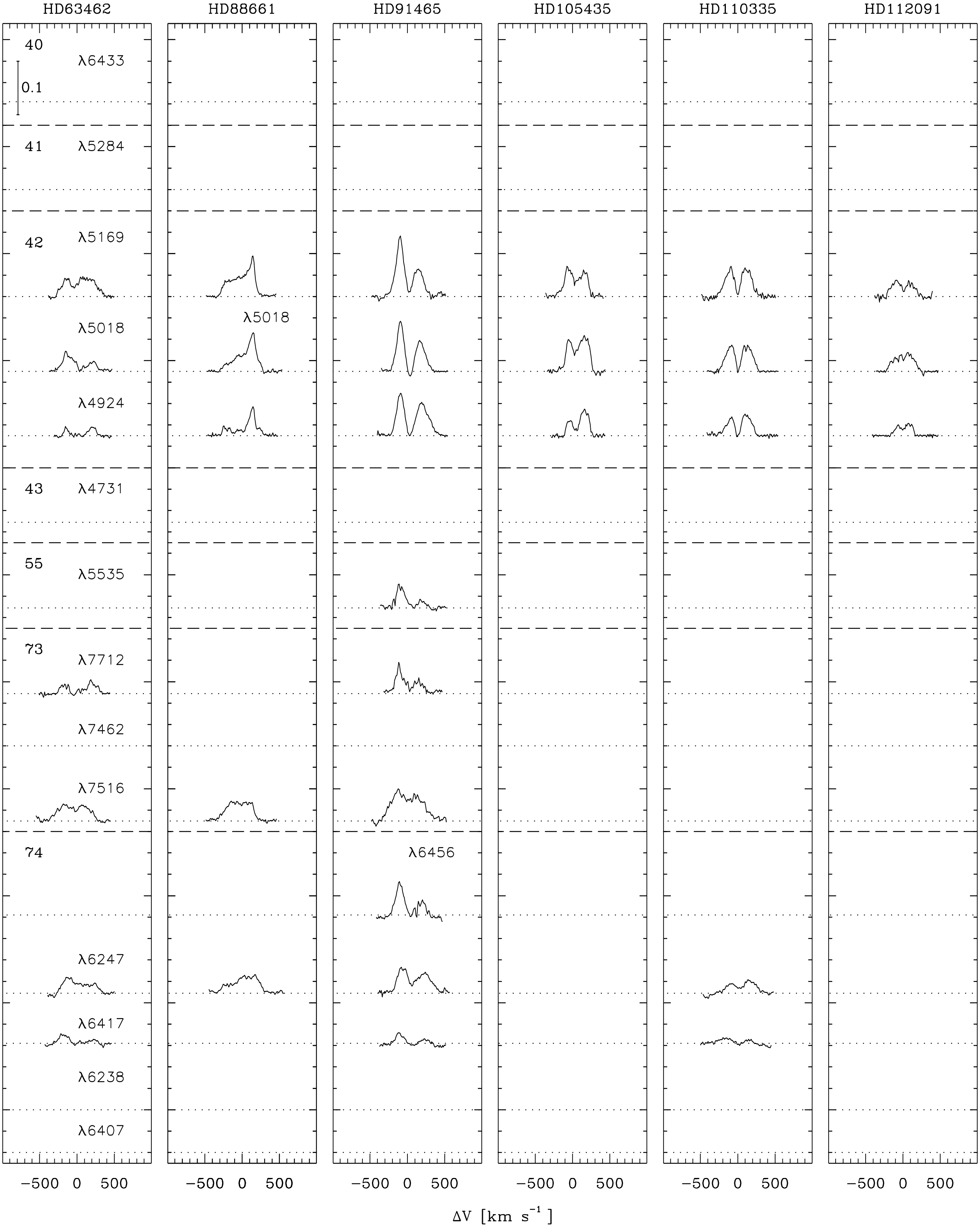

Fig. 10. Same as in Fig. 7.

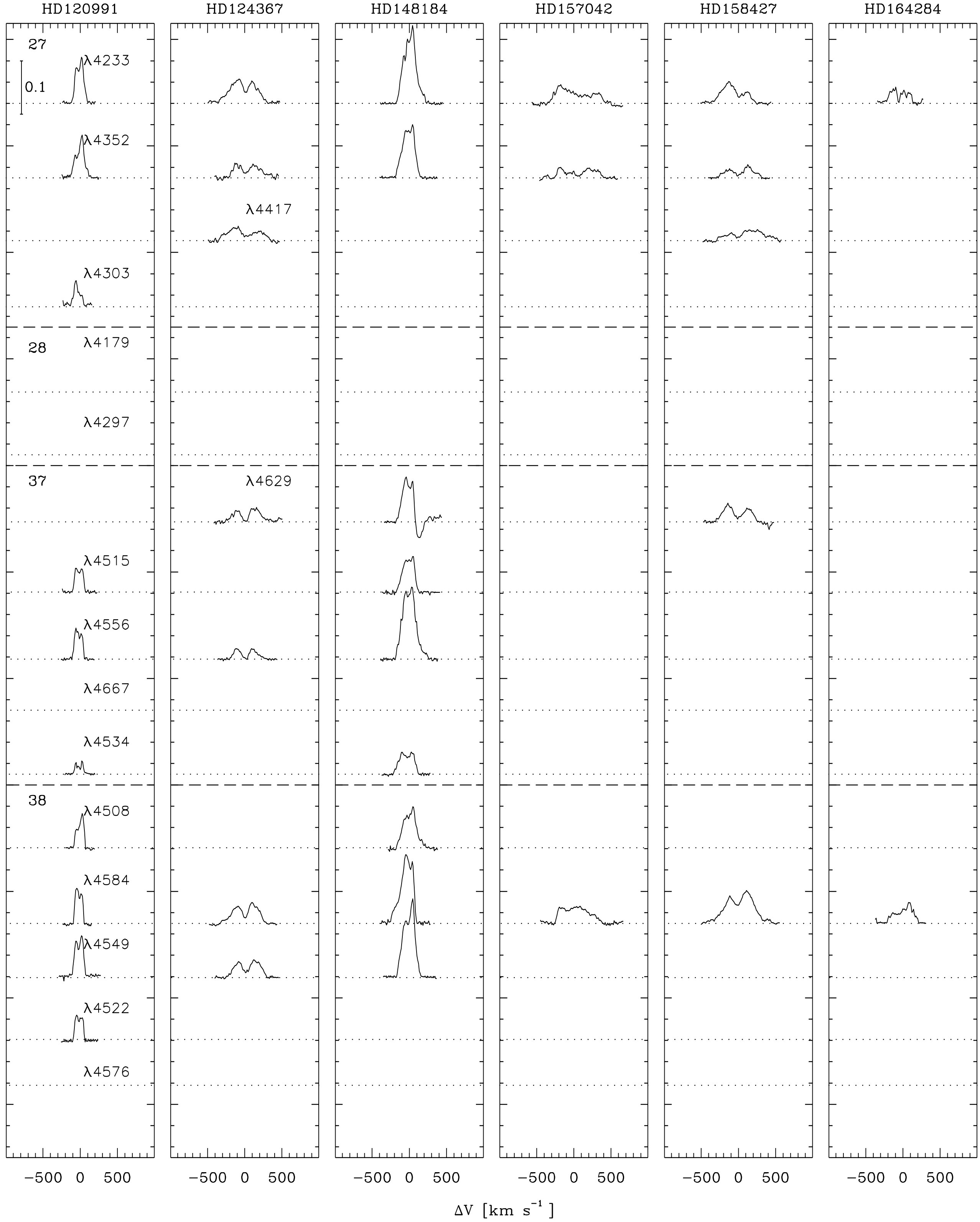

Fig. 11. Same as in Fig. 7.

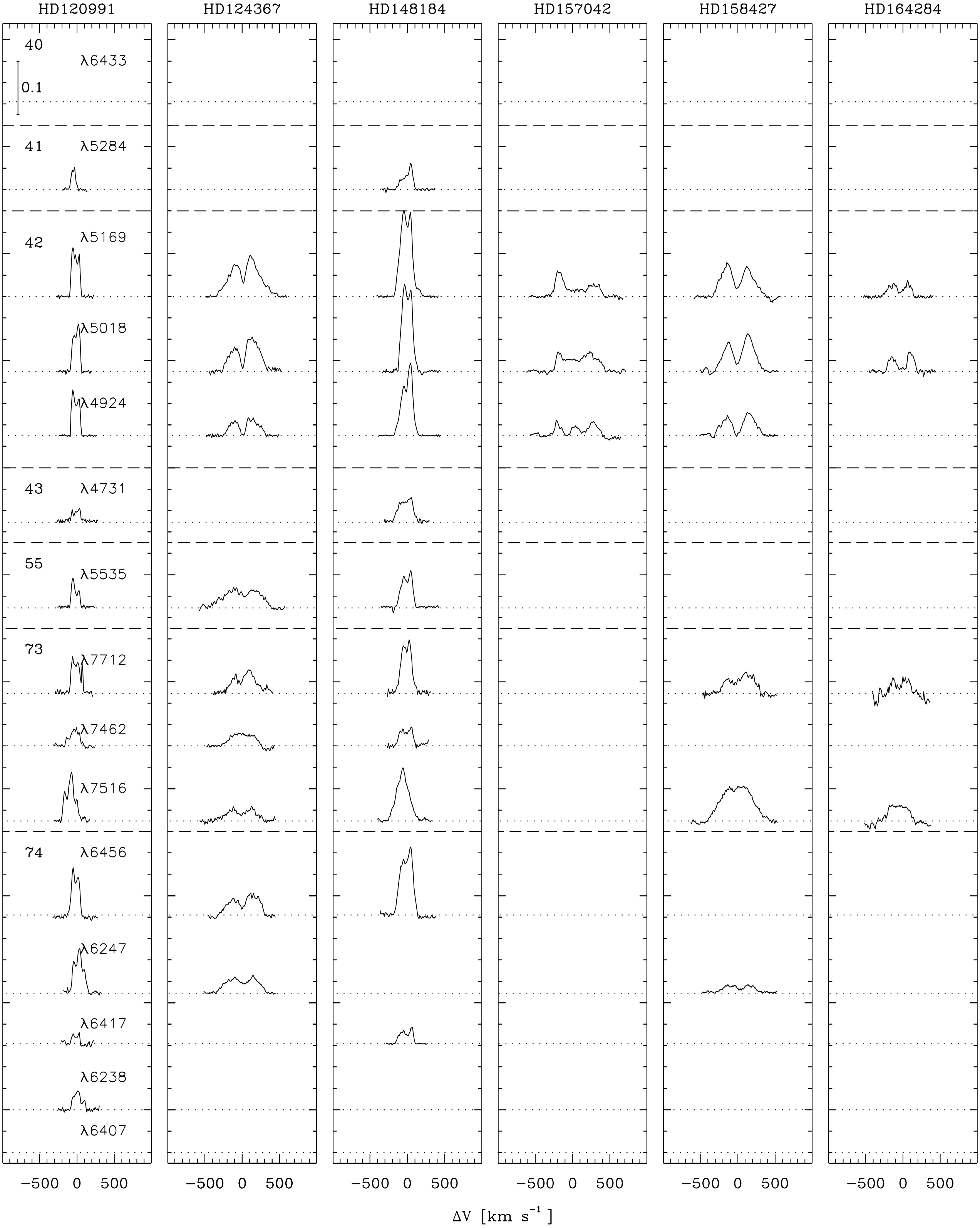

Fig. 12. Same as in Fig. 7.

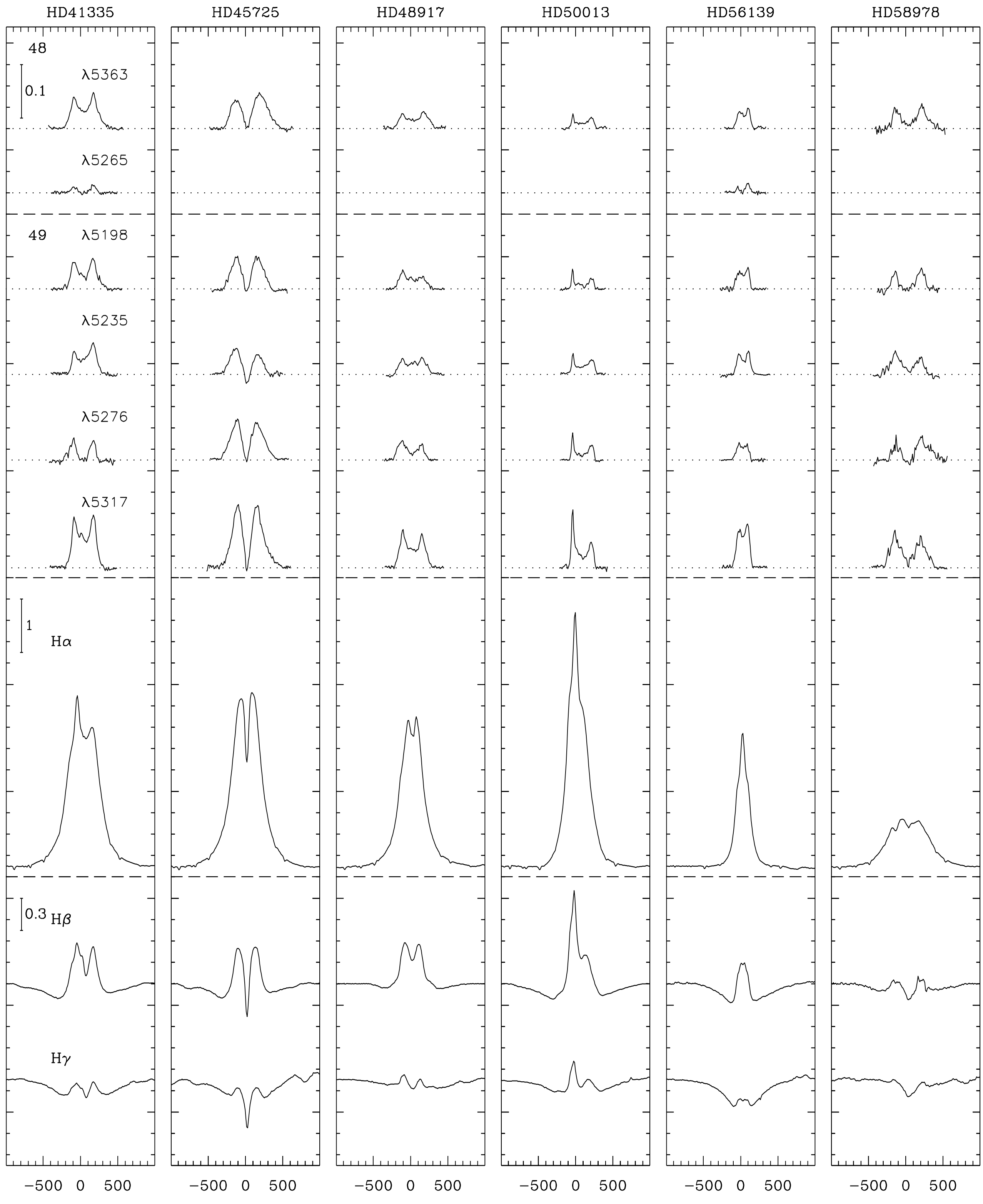

Fig. 13. Fe II and Balmer line emission profiles of some observed Be stars. The number in the upper left hand corner of each column of Fe II line profiles indicates the line multiplet. Hβ and Hγ lines have the same intensity scales, but it is different for Hα.

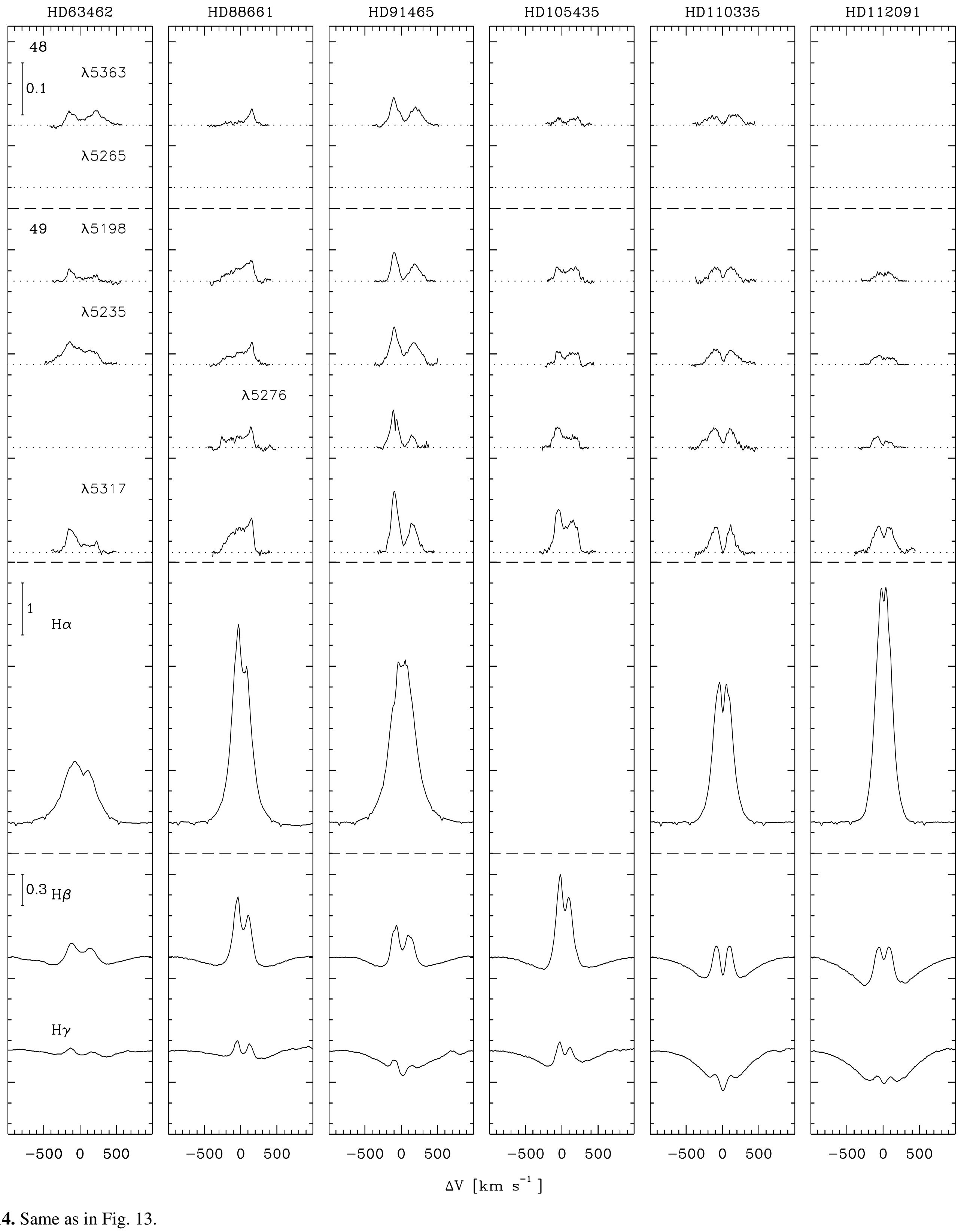

Fig. 14. Same as in Fig. 13.

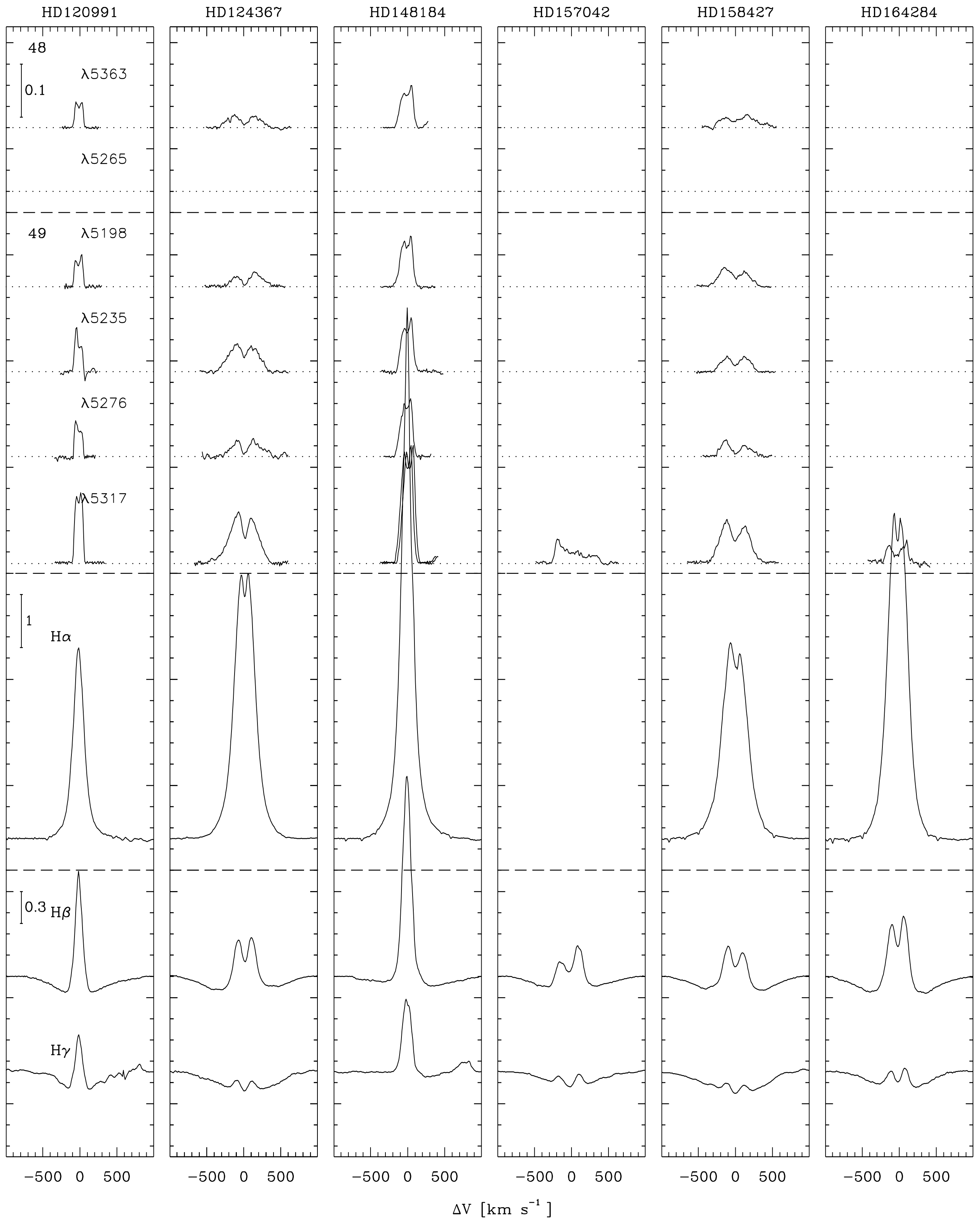

Fig. 15. Same as in Fig. 13.

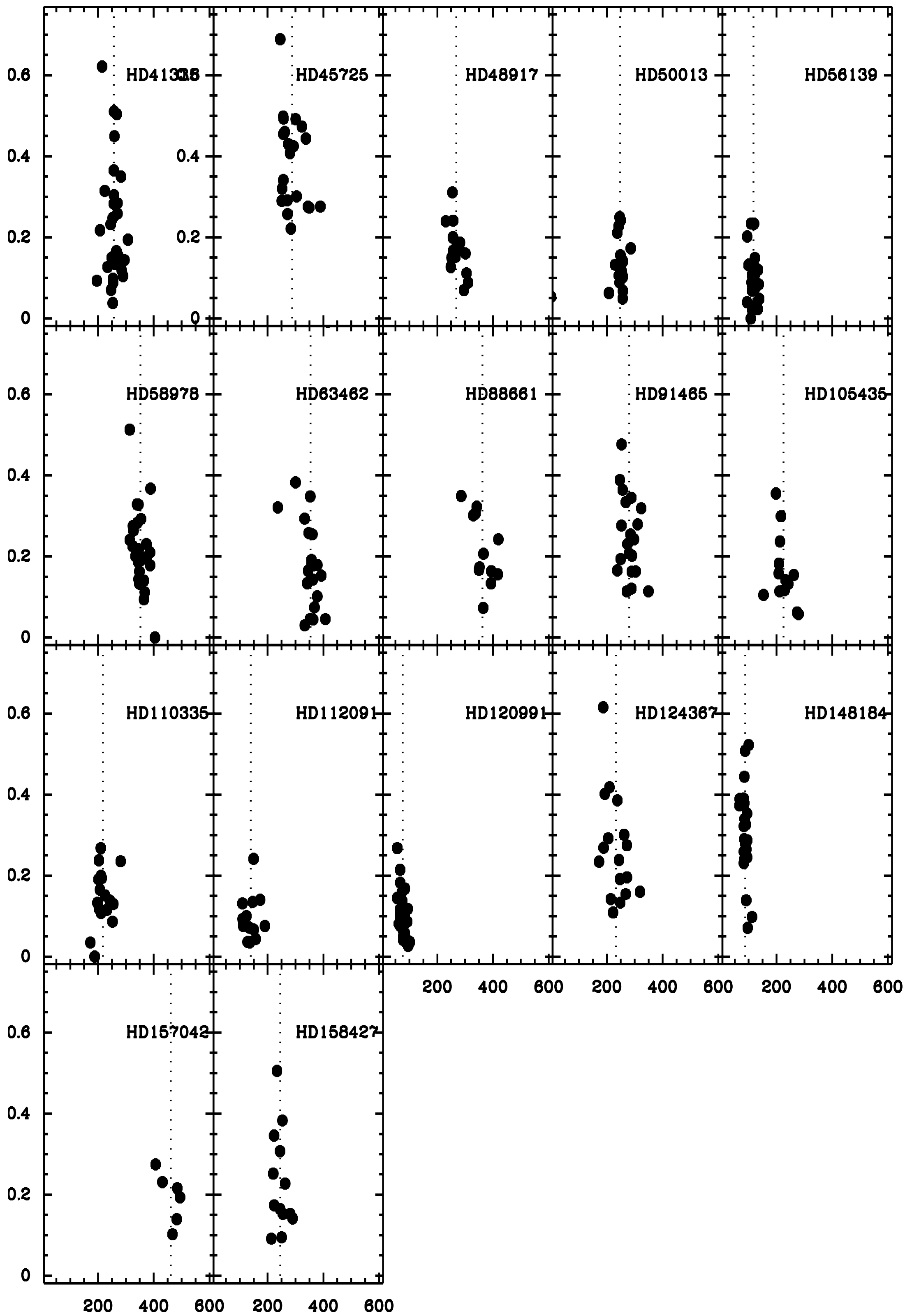

Fig. 16. Equivalent widths W (Å) of individual Fe II emission lines against their peak separation Δ_p (km s^{-1}) in all observed Be stars.

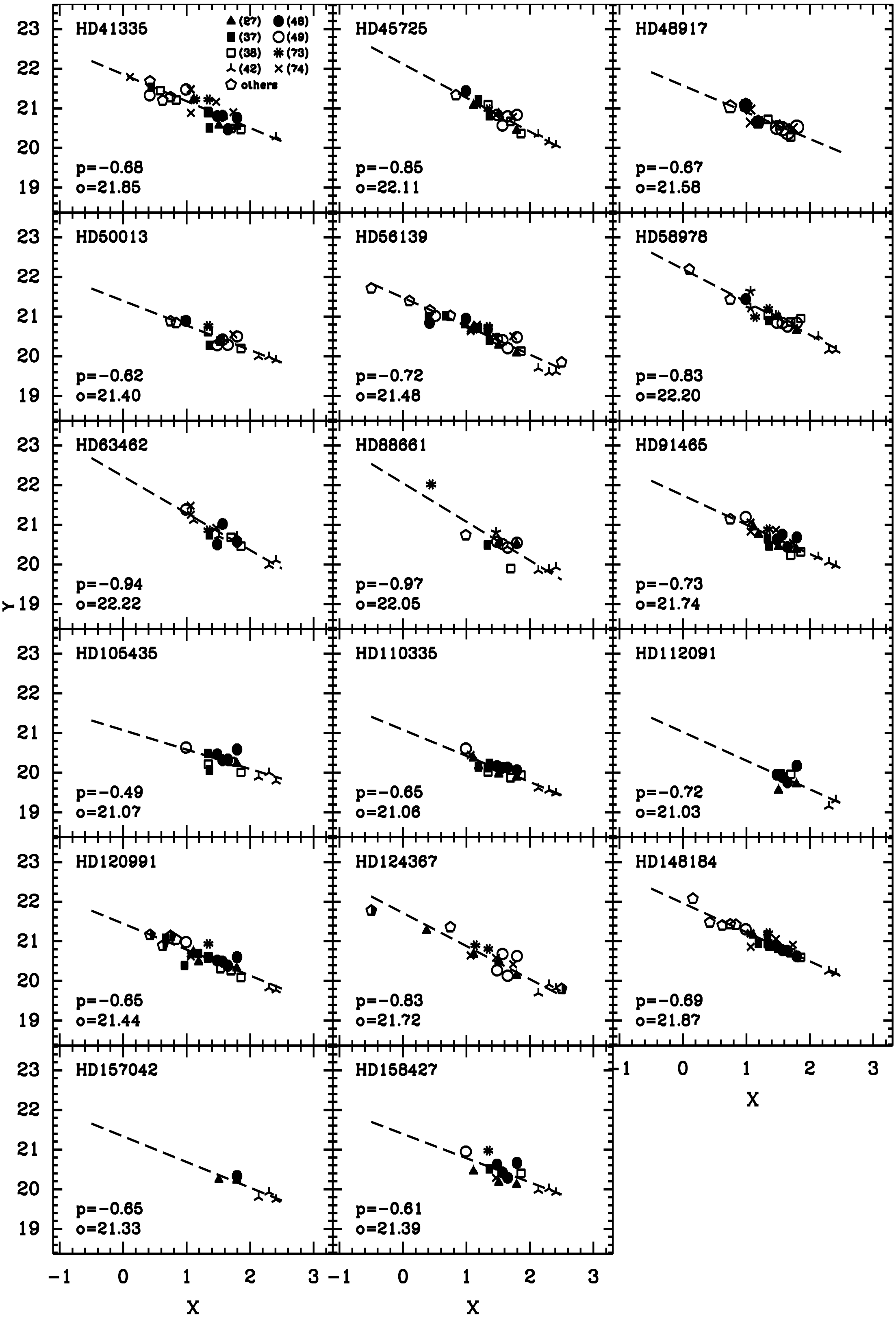

Fig. 17. Empirical SAC slopes for all observed Be stars. Each symbol corresponds to a given multiplet. The correspondence between symbols and multiplets is shown in the first left upper panel. In each panel are also given the slope $p = \partial Y/\partial X$ and o = ordinate at $X = 0$.

Table 4. Journal and spectral ranges of spectroscopic observations.

HD	Date [dd/mm/yy]	Spectral Range [Angstroms]	Julian Date [days]
41335	05/03/96	3900–6450	2 450 148.533
	06/03/96	5600–8100	2 450 149.518
45725	07/03/96	3900–6450	2 450 150.506
		5600–8100	2 450 150.666
47054	07/03/96	3900–6450	2 450 150.523
		5600–8100	2 450 150.681
48917	07/03/96	3900–6450	2 450 150.554
		5600–8100	2 450 150.696
50013	05/03/96	3900–6450	2 450 148.579
	06/03/96	5600–8100	2 450 149.572
56139	07/03/96	3900–6450	2 450 150.609
		5600–8100	2 450 150.732
58978	07/03/96	3900–6450	2 450 150.622
		5600–8100	2 450 150.743
63462	05/03/96	3900–6450	2 450 148.635
	06/03/96	5600–8100	2 450 149.629
88661	05/03/96	3900–6450	2 450 148.655
	06/03/96	5600–8100	2 450 149.648
91465	05/03/96	3900–6450	2 450 148.691
	06/03/96	5600–8100	2 450 149.685
105435	05/03/96	3900–6450	2 450 148.704
	06/03/96	5600–8100	2 450 149.700
110335	07/03/96	3900–6450	2 450 150.806
		5600–8100	2 450 150.862
112091	07/03/96	3900–6450	2 450 150.821
		5600–8100	2 450 150.891
120991	05/03/96	3900–6450	2 450 148.877
	06/03/96	5600–8100	2 450 149.876
124367	05/03/96	3900–6450	2 450 148.777
	06/03/96	5600–8100	2 450 149.769
148184	05/03/96	3900–6450	2 450 148.828
	06/03/96	5600–8100	2 450 149.825
	21/09/96	3700–6150	2 450 348.521
	22/09/96	5850–8100	2 450 349.527
157042	21/09/96	3700–6150	2 450 348.478
158427	21/09/96	3700–6150	2 450 348.508
	22/09/96	5850–8100	2 450 349.551
164284	21/09/96	3700–6150	2 450 348.557
	22/09/96	5850–8100	2 450 349.569

Table 5. Measurements of the observed Fe II emission lines.

Multiplet	λ Å	I_b	I_r	I_{cd}	D_p (km s^{-1})	$D_{1/2}$ (km s^{-1})	D_1 (km s^{-1})	W_λ Å
				HD 41335				
27	4233.172	1.064	1.061	1.044	224	350	625	−0.3145
27	4351.769	—	—	—	—	—	—	−0.1701
27	4416.830	1.017	1.034	—	285	—	426	−0.1185
37	4555.893	1.035	1.033	1.011	207	356	429	−0.2175
37	4629.339	1.038	1.038	1.000	253	—	—	−0.0979
37	4666.758	1.018	1.031	1.010	234	—	435	−0.1271
38	4508.288	1.047	1.050	1.029	245	385	457	−0.2321
38	4549.474	1.032	1.059	1.019	282	435	541	−0.3498
38	4576.340	1.031	1.039	1.013	249	362	436	−0.1499
38	4583.837	1.055	1.078	1.027	256	350	545	−0.2830
40	6432.628	1.066	1.064	1.031	220	363	494	−0.3314
41	5284.109	1.040	1.047	1.015	265	334	436	−0.1603
42	4923.927	1.052	1.057	1.003	245	338	440	−0.1733
42	5018.440	1.048	1.079	1.022	259	315	591	−0.2812
42	5169.033	1.101	1.120	1.067	214	346	472	−0.6215
43	4731.453	1.023	1.025	1.005	254	357	452	−0.0880
48	5264.812	1.013	1.022	1.002	246	347	440	−0.0702
48	5362.869	1.055	1.072	1.032	256	390	546	−0.3652
49	5197.577	1.049	1.057	1.023	252	354	427	−0.2477
49	5234.625	1.049	1.068	1.033	257	359	475	−0.3039
49	5276.002	1.045	1.045	1.005	266	361	421	−0.1659
49	5316.615	1.094	1.097	1.046	258	334	461	−0.4496
55	5534.847	1.045	1.037	1.002	265	350	423	−0.1339
73	7462.407	1.039	1.041	1.016	269	388	465	−0.2586
73	7515.831	1.072	0	0	268	477	846	−0.7788
73	7711.723	1.052	1.053	1.019	269	338	423	−0.2844
74	6147.741	—	—	—	—	—	—	−0.2991
74	6149.258	—	—	—	—	—	—	−0.2991
74	6247.557	1.059	1.071	1.040	267	417	574	−0.5041
74	6407.251	1.015	1.013	1.007	195	—	457	−0.0930
74	6416.919	1.019	1.023	1.004	289	385	506	−0.1047
74	6456.383	1.073	1.090	1.038	257	349	472	−0.5106
				HD 45725				
27	4233.172	1.075	1.063	1.000	251	443	653	−0.3204
27	4351.769	1.082	1.074	1.000	273	523	721	−0.4304
27	4416.830	1.041	1.056	1.000	389	607	761	−0.2760
37	4515.339	1.069	1.074	1.000	337	589	735	−0.4438
37	4629.339	1.049	1.064	1.000	271	433	581	−0.2573
38	4508.288	1.062	1.077	1.013	322	668	884	−0.4735
38	4549.474	1.070	1.082	0.990	280	502	694	−0.4081
38	4583.837	1.062	1.086	0.980	270	422	560	−0.2913
42	4923.927	1.084	1.102	0.990	256	434	642	−0.4931
42	5018.440	1.095	1.094	0.980	261	435	595	−0.4600
42	5169.033	1.092	1.103	0.990	255	395	549	−0.4982
43	4731.453	1.020	1.033	0.994	334	514	716	−0.1500
48	5362.869	1.051	1.065	1.002	292	535	748	−0.4249
49	5197.577	1.059	1.060	0.990	256	466	643	−0.3414
49	5234.625	1.049	1.036	0.990	283	469	606	−0.2214
49	5276.002	1.076	1.070	1.000	256	478	748	−0.4551
49	5316.615	1.117	1.112	0.990	245	429	641	−0.6889
55	5534.847	1.028	1.067	1.000	292	464	620	−0.3299
73	7515.831	1.050	1.051	0	250	474	799	−0.5811
73	7711.723	1.047	1.045	1.000	250	360	525	−0.2900
74	6238.392	1.030	1.037	1.000	349	577	790	−0.2733
74	6247.557	1.033	1.047	1.000	303	501	622	−0.3013
74	6416.919	1.034	1.024	1.000	367	571	776	−0.2524
74	6456.383	1.062	1.069	1.000	300	498	632	−0.4919

Table 5. continued.

Multiplet	λ Å	I_b	I_r	I_{cd}	D_p km s^{-1}	$D_{1/2}$ km s^{-1}	D_1 km s^{-1}	W_λ Å
				HD 48917				
27	4233.172	1.059	1.042	—	257	365	503	−0.2410
27	4351.769	1.041	1.041	1.018	269	458	681	−0.2268
37	4515.339	1.021	1.035	1.006	304	424	461	−0.1113
37	4629.339	1.030	1.034	1.014	283	377	455	−0.1342
38	4508.288	1.028	1.036	—	281	413	483	−0.1868
38	4549.474	1.041	1.014	—	264	—	487	−0.1511
38	4583.837	1.052	1.041	1.014	256	403	495	−0.1985
42	4923.927	1.033	1.036	0.999	253	331	457	−0.0974
42	5018.440	1.041	1.038	1.005	213	334	466	−0.1587
42	5169.033	1.044	1.039	1.008	260	346	489	−0.1679
48	5362.869	1.028	1.032	1.013	278	428	521	−0.1710
49	5197.577	1.036	1.020	—	250	377	484	−0.1497
49	5234.625	1.030	1.032	—	257	401	507	−0.1678
49	5276.002	1.036	1.031	1.011	265	368	472	−0.1601
49	5316.615	1.069	1.063	1.031	254	358	498	−0.3108
55	5534.847	1.024	1.015	1.006	310	360	412	−0.0883
73	7515.831	1.048	1.052	1.036	210	419	608	−0.5070
73	7711.723	1.029	1.022	0	243	331	399	−0.1185
74	6147.741	—	—	—	—	—	—	−0.1504
74	6149.258	—	—	—	—	—	—	−0.1504
74	6247.557	1.023	1.020	1.012	301	415	474	−0.1601
74	6416.919	1.013	1.011	1.000	295	—	532	−0.0698
74	6456.383	1.038	1.033	—	230	391	477	−0.2396
				HD 50013				
27	4233.172	1.089	1.032	—	246	362	440	−0.2497
27	4351.769	1.041	1.032	—	242	310	360	−0.1056
28	4178.862	1.020	1.019	—	207	269	306	−0.0626
37	4629.339	—	—	—	—	—	360	−0.0533
38	4508.288	1.031	1.022	—	253	332	410	−0.1154
38	4522.634	1.033	1.028	—	257	306	359	−0.1029
38	4583.837	1.059	1.043	1.013	257	306	375	−0.1407
42	4923.927	1.049	1.059	1.008	248	312	365	−0.1559
42	5018.440	—	—	—	—	—	—	−0.2293
42	5169.033	1.073	1.071	1.024	249	305	379	−0.2419
48	5362.869	1.030	1.022	1.011	245	304	377	−0.0884
49	5197.577	1.035	1.018	1.007	257	306	358	−0.0675
49	5234.625	1.039	1.027	1.014	247	312	373	−0.1123
49	5276.002	1.051	1.027	1.008	255	298	348	−0.1006
49	5316.615	1.110	1.049	1.022	242	292	375	−0.2278
55	5534.847	1.032	1.009	1.004	256	268	336	−0.0492
73	7515.831	1.044	1.035	0	216	353	570	−0.3399
73	7711.723	1.052	1.015	—	229	—	338	−0.1323
74	6456.383	1.046	1.040	—	237	323	429	−0.2110
				HD 56139				
27	4233.172	1.037	1.049	—	119	181	279	−0.1071
27	4303.176	1.015	1.010	—	113	166	207	−0.0204
27	4351.769	—	—	—	122	184	262	−0.0856
27	4416.830	1.029	1.031	1.022	111	188	290	−0.0844
28	4296.572	1.014	1.015	1.004	119	179	225	−0.0277
37	4515.339	1.034	1.044	—	122	207	289	−0.1086
37	4534.168	1.011	1.021	1.007	129	199	232	−0.0337
37	4555.893	1.042	1.037	1.032	119	223	278	−0.1303
37	4629.339	1.029	1.038	1.015	118	177	232	−0.0783
38	4508.288	1.038	1.057	1.032	122	203	332	−0.1489
38	4549.474	1.064	1.081	1.055	119	204	306	−0.2335
38	4583.837	1.044	1.045	—	113	181	281	−0.1294
40	6432.628	1.009	1.015	1.008	131	189	239	−0.0419
41	5284.109	1.011	1.023	1.010	138	191	218	−0.0481
42	4923.927	1.020	1.027	1.007	94	139	171	−0.0399
42	5018.440	1.079	1.046	1.034	118	181	232	−0.9890
42	5169.033	1.053	1.041	1.023	99	186	253	−0.1313

Table 5. continued.

Multiplet	λ Å	I_b	I_r	I_{cd}	D_p km s^{-1}	$D_{1/2}$ km s^{-1}	D_1 km s^{-1}	W_λ Å
48	5264.812	1.013	1.017	0.997	132	179	234	−0.0229
48	5362.869	1.032	1.038	1.024	118	187	281	−0.1081
49	5197.577	1.034	1.041	1.024	112	182	250	−0.1060
49	5234.625	1.039	1.044	1.025	133	188	261	−0.1198
49	5276.002	1.033	1.031	1.021	110	172	262	−0.0889
49	5316.615	1.069	1.080	1.056	108	189	273	−0.2340
55	5534.847	1.021	1.030	1.013	121	186	246	−0.0721
73	7462.407	—	1.019	—	114	209	243	−0.0767
73	7515.831	0	0	0	84	229	389	−0.2354
73	7711.723	1.025	1.030	1.022	100	197	238	−0.1329
74	6147.741	—	—	—	—	—	—	−0.0601
74	6149.258	—	—	—	—	—	—	−0.0601
74	6238.392	1.020	1.031	—	111	201	324	−0.1068
74	6247.557	1.023	1.031	1.021	112	200	272	−0.1063
74	6416.919	1.014	1.022	—	111	195	247	−0.0688
74	6456.383	1.049	1.054	1.046	94	189	266	−0.2021
HD 58978								
27	4233.172	1.046	1.043	1.021	324	479	606	−0.2249
27	4351.769	1.041	1.042	1.000	327	475	708	−0.2637
37	4629.339	1.032	1.039	1.000	345	435	536	−0.1439
38	4508.288	1.035	1.036	1.005	344	471	573	−0.1866
38	4549.474	1.047	1.047	1.000	354	559	589	−0.2925
38	4583.837	1.088	1.061	1.034	313	544	666	−0.5131
40	6432.628	1.024	1.030	1.001	364	477	546	−0.1404
42	4923.927	1.053	1.066	1.005	340	527	748	−0.3284
42	5018.440	1.028	1.060	1.002	386	—	608	−0.2098
42	5169.033	1.055	1.040	1.008	325	475	526	−0.2753
48	5362.869	1.036	1.047	1.006	334	463	499	−0.2006
49	5197.577	1.031	1.038	1.000	348	455	548	−0.1628
49	5234.625	1.044	1.032	1.005	344	450	583	−0.1918
49	5276.002	1.029	1.040	1.000	352	550	610	−0.1903
49	5316.615	1.067	1.057	1.001	345	467	582	−0.3281
55	5534.847	1.032	1.030	1.000	367	427	465	−0.1117
73	7462.407	1.018	1.015	1.000	364	484	572	−0.0943
73	7515.831	1.028	1.030	1.007	341	528	680	−0.2829
73	7711.723	1.036	1.036	1.002	313	426	580	−0.2408
74	6149.258	1.027	1.052	1.008	388	—	684	−0.3674
74	6247.557	1.035	1.030	1.004	373	539	611	−0.2305
74	6416.919	1.018	1.024	1.006	357	475	591	−0.1377
74	6456.383	1.037	1.051	1.000	346	479	580	−0.2174
HD 63462								
27	4233.172	1.053	1.017	—	347	430	684	−0.2581
27	4303.176	1.016	1.007	0	407	0	585	−0.0454
27	4351.769	1.013	1.007	—	332	—	480	−0.0299
27	4416.830	1.016	1.020	1.008	341	—	721	−0.1339
37	4555.893	1.037	1.012	0	403	0	640	−0.1738
37	4629.339	1.031	1.015	0	351	478	581	−0.1281
38	4549.474	1.032	1.036	1.011	357	502	606	−0.1915
38	4583.837	1.031	1.031	1.007	344	506	723	−0.1645
42	4923.927	1.017	1.015	0.999	363	434	479	−0.0444
42	5018.440	1.038	1.017	1.003	362	460	524	−0.1429
42	5169.033	1.034	1.035	1.018	284	501	649	−0.2583
48	5362.869	1.025	1.028	1.011	378	503	622	−0.1788
49	5197.577	1.023	1.011	1.004	367	428	512	−0.0743
49	5234.625	1.044	1.025	—	332	520	697	−0.2934
49	5316.615	1.042	1.021	1.012	364	444	538	−0.1777
73	7515.831	1.029	1.029	1.022	236	473	644	−0.3212
73	7711.723	1.016	1.023	1.000	344	524	561	−0.1118
74	6149.258	1.028	1.029	1.013	360	544	633	−0.2547
74	6247.557	1.026	1.016	1.012	357	485	607	−0.1796
74	6416.919	1.027	1.015	1.000	392	—	560	−0.1526

Table 5. continued.

Multiplet	λ Å	I_b	I_r	I_{cd}	D_p (km s^{-1})	$D_{1/2}$ (km s^{-1})	D_1 (km s^{-1})	W_λ Å
				HD 88661				
27	4233.172	1.037	1.060	—	341	459	544	−0.3227
27	4351.769	1.019	1.045	—	351	432	547	−0.1734
37	4629.339	1.033	1.012	0	373	0	577	−0.1121
38	4508.288	1.039	1.006	0	296	0	585	−0.1385
42	4923.927	1.018	1.054	—	392	—	479	−0.1334
42	5018.440	1.007	1.069	—	365	—	526	−0.2065
42	5169.033	1.028	1.075	—	336	421	575	−0.3063
48	5362.869	1.007	1.031	—	365	—	495	−0.0729
49	5197.577	1.007	1.034	—	417	—	497	−0.1557
49	5234.625	1.016	1.042	—	349	—	541	−0.1669
49	5276.002	1.021	1.039	—	393	—	506	−0.1635
49	5316.615	1.029	1.064	—	329	369	493	−0.3013
73	7515.831	1.035	1.034	—	286	403	509	−0.3490
74	6247.557	1.014	1.032	—	419	518	583	−0.2423
				HD 91465				
27	4233.172	1.087	1.033	1.017	252	390	563	−0.2763
27	4303.176	1.034	1.030	1.004	303	500	661	−0.1631
27	4351.769	1.051	1.029	1.000	288	404	600	−0.1625
27	4416.830	1.036	1.030	1.011	290	498	686	−0.2019
37	4555.893	1.063	1.020	1.001	237	—	—	−0.1655
37	4629.339	1.049	1.022	0.994	271	362	520	−0.1138
38	4549.474	1.064	—	1.000	104	—	—	−0.1458
38	4583.837	1.073	1.051	0.992	284	423	587	−0.2545
42	4923.927	1.094	1.050	1.000	287	406	592	−0.3448
42	5018.440	1.115	1.051	1.000	256	378	571	−0.3643
42	5169.033	1.108	1.056	1.006	246	375	576	−0.3888
48	5362.869	1.054	1.036	1.008	297	434	669	−0.2423
49	5197.577	1.054	1.033	1.002	279	391	575	−0.2076
49	5234.625	1.072	1.041	1.016	267	425	615	−0.3342
49	5276.002	1.071	1.025	1.000	249	316	474	−0.1938
49	5316.615	1.127	1.056	1.016	252	459	608	−0.4766
55	5534.847	1.042	1.014	1.000	288	359	497	−0.1208
73	7515.831	1.060	1.040	1.037	233	515	689	−0.5881
73	7711.723	1.056	1.028	1.001	273	—	476	−0.2306
74	6147.741	—	—	—	—	—	—	−0.1954
74	6149.258	—	—	—	—	—	—	−0.1954
74	6247.557	1.047	1.037	1.011	323	451	656	−0.3189
74	6416.919	1.024	1.011	1.000	349	480	586	−0.1139
74	6456.383	1.066	1.033	1.001	310	411	569	−0.2792
				HD 105435				
27	4233.172	1.048	1.034	—	208	352	407	−0.1822
27	4351.769	1.035	1.029	—	213	343	470	−0.1381
37	4555.893	1.026	1.024	1.014	153	323	381	−0.1049
37	4629.339	1.021	1.011	1.000	229	313	346	−0.0428
38	4508.288	1.017	1.009	—	278	—	354	−0.0579
38	4522.634	1.014	1.007	0	279	336	352	−0.0250
38	4549.474	1.042	1.028	1.017	261	372	429	−0.1541
38	4583.837	1.029	1.037	1.014	228	331	394	−0.1166
42	4923.927	1.026	1.048	1.010	207	319	380	−0.1582
42	5018.440	1.058	1.062	1.036	216	344	416	−0.2992
42	5169.033	1.052	1.047	1.028	212	330	398	−0.2370
48	5362.869	1.015	1.014	1.004	274	360	383	−0.0617
49	5197.577	1.027	1.027	1.017	242	342	383	−0.1321
49	5234.625	1.022	1.022	1.012	210	336	363	−0.1139
49	5276.002	1.037	1.022	1.018	232	325	406	−0.1419
49	5316.615	1.081	1.060	1.048	198	332	414	−0.3554

Table 5. continued.

Multiplet	λ Å	I_b	I_r	I_{cd}	D_p	$D_{1/2}$ km s^{-1}	D_1	W_λ Å
				HD 110335				
27	4233.172	1.038	1.035	1.013	213	457	582	−0.1938
27	4303.176	1.018	1.020	—	294	423	490	−0.0918
27	4351.769	1.024	1.021	1.002	204	487	574	−0.1175
27	4416.830	1.016	1.017	1.005	231	—	744	−0.1151
37	4515.339	1.016	1.015	0.995	285	498	600	−0.0809
37	4555.893	1.035	1.024	1.010	210	308	367	−0.1078
37	4629.339	1.034	1.041	1.008	187	337	427	−0.1438
38	4508.288	1.012	1.019	0.998	252	506	604	−0.0862
38	4549.474	1.036	1.040	1.005	242	386	415	−0.1387
38	4583.837	1.040	1.043	0.999	281	466	529	−0.2354
42	4923.927	1.030	1.043	0.998	201	375	449	−0.1908
42	5018.440	1.046	1.048	1.000	202	398	532	−0.2469
42	5169.033	1.056	1.049	1.004	210	381	503	−0.2678
48	5362.869	1.017	1.020	1.002	255	478	584	−0.1299
49	5197.577	1.028	1.028	1.007	225	373	541	−0.1510
49	5234.625	1.029	1.026	1.006	207	410	526	−0.1651
49	5276.002	1.037	1.037	1.009	210	382	567	−0.1995
49	5316.615	1.048	1.052	0.997	203	336	505	−0.2375
74	6247.557	1.015	1.023	1.007	225	420	505	−0.1276
74	6416.919	1.014	1.011	1.001	301	510	563	−0.0955
				HD 112091				
27	4233.172	1.029	1.028	1.021	123	272	380	−0.1001
27	4351.769	1.016	1.017	1.004	136	251	287	−0.0353
38	4522.634	1.023	1.017	1.015	109	321	427	−0.0928
38	4549.474	1.026	1.029	1.014	109	—	—	−0.1312
38	4583.837	1.012	1.014	0.999	124	280	339	−0.0345
42	4923.927	1.020	1.023	1.012	142	260	335	−0.0751
42	5018.440	1.016	1.016	1.002	190	354	405	−0.0757
42	5169.033	1.031	1.028	1.009	173	342	432	−0.1402
49	5197.577	1.014	1.017	1.013	133	271	390	−0.0720
49	5234.625	1.017	1.013	—	111	346	399	−0.0763
49	5276.002	1.020	1.012	1.004	149	290	345	−0.0666
49	5316.615	1.049	1.047	1.026	149	302	432	−0.2412
				HD 120991				
27	4233.172	1.066	1.085	1.060	73	129	236	−0.1592
27	4303.176	1.046	1.019	1.018	83	127	190	−0.0576
27	4351.769	1.041	1.084	1.036	93	153	182	−0.1178
28	4178.862	1.083	—	—	76	—	236	−0.0927
37	4515.339	1.047	1.045	1.037	74	131	185	−0.0879
37	4520.224	1.036	1.035	1.031	77	127	165	−0.0642
37	4534.168	1.021	1.024	1.009	89	121	167	−0.0328
37	4555.893	1.061	1.050	1.040	67	124	163	−0.0933
38	4508.288	1.041	1.067	1.037	77	132	155	−0.1031
38	4522.634	1.048	1.041	1.035	62	124	157	−0.0810
38	4549.474	1.066	1.076	1.051	74	134	185	−0.1373
38	4583.837	1.065	1.054	1.047	67	119	143	−0.1029
41	5284.109	—	—	—	—	—	—	−0.0416
42	4923.927	1.085	1.068	1.056	86	127	154	−0.1413
42	5018.440	1.067	1.088	1.063	55	118	152	−0.1446
42	5169.033	1.091	1.076	1.061	83	126	163	−0.1679
43	4731.453	1.022	1.024	1.010	99	124	154	−0.0370
48	5362.869	1.049	1.047	1.036	83	121	181	−0.0995
49	5197.577	1.049	1.059	1.040	78	125	174	−0.1087
49	5234.625	1.082	1.047	1.044	73	115	155	−0.1226
49	5276.002	1.067	1.048	1.047	66	122	146	−0.1165
49	5316.615	1.125	1.132	1.112	56	124	182	−0.2680
49	5325.553	1.022	1.021	1.013	101	126	148	−0.0359

Table 5. continued.

Multiplet	λ Å	I_b	I_r	I_{cd}	D_p	$D_{1/2}$ km s^{-1}	D_1	W_λ Å
55	5534.847	1.052	1.031	1.022	82	122	156	−0.0815
73	7462.407	0	0	0	0	0	256	−0.1158
73	7515.831	0	0	0	0	0	262	−0.2902
73	7711.723	1.067	1.056	1.048	67	124	159	−0.1826
74	6147.741	—	—	—	—	—	—	−0.0582
74	6149.258	—	—	—	—	—	—	−0.0582
74	6238.392	1.023	1.035	1.025	67	119	151	−0.0757
74	6247.557	1.056	1.080	1.048	79	170	263	−0.2217
74	6416.919	1.022	1.025	1.015	77	118	156	−0.0492
74	6456.383	1.092	1.075	1.063	66	123	196	−0.2143
				HD 124367				
27	4233.172	1.045	1.042	1.021	171	427	672	−0.2342
27	4273.326	1.045	—	—	74	—	—	−0.1209
27	4351.769	1.033	1.059	1.018	271	466	533	−0.2748
27	4416.830	1.026	1.020	1.011	318	596	714	−0.1599
37	4555.893	1.020	1.018	1.000	224	338	485	−0.0737
37	4629.339	1.020	1.025	1.001	222	410	575	−0.1089
38	4549.474	1.032	1.036	1.012	210	435	630	−0.1800
38	4583.837	1.032	1.032	1.009	272	458	586	−0.1956
42	4923.927	1.028	1.032	1.002	239	455	568	−0.1613
42	5018.440	1.046	1.072	1.008	237	529	633	−0.3856
42	5169.033	1.051	1.071	1.018	192	416	714	−0.4015
48	5362.869	1.025	1.021	1.005	267	507	618	−0.1544
49	5197.577	1.019	1.025	1.002	248	439	560	−0.1332
49	5234.625	1.056	1.053	1.030	209	461	729	−0.4179
49	5276.002	1.023	1.028	0.999	213	354	626	−0.1422
49	5316.615	1.094	1.094	1.046	186	420	735	−0.6153
55	5534.847	1.040	1.031	1.022	204	612	715	−0.2919
73	7462.407	—	—	—	—	—	—	−0.2088
73	7515.831	1.026	1.026	1.008	246	381	558	−0.1915
73	7711.723	1.034	1.041	1.015	188	321	405	−0.2688
74	6147.741	—	—	—	—	—	—	−0.1096
74	6149.258	—	—	—	—	—	—	−0.1096
74	6247.557	1.028	1.032	1.016	243	479	653	−0.2384
74	6456.383	1.037	1.041	1.016	261	438	540	−0.3006
				HD 148184				
27	4173.461	1.080	1.077	1.066	91	226	364	−0.265
27	4233.172	1.120	1.146	1.114	67	191	415	−0.373
27	4351.769	1.045	1.068	1.048	88	142	316	−0.278
37	4515.339	1.062	1.068	0	94	188	315	−0.192
37	4534.168	1.041	1.038	1.032	119	244	351	−0.140
37	4555.893	1.132	1.134	1.122	82	210	380	−0.390
37	4629.339	1.084	1.075	1.063	82	173	262	−0.231
38	4508.288	1.067	1.082	1.060	83	218	389	−0.259
38	4549.474	1.104	1.143	1.097	94	189	316	−0.353
38	4583.837	1.129	1.116	1.101	84	186	373	−0.379
41	5284.109	0	1.049	0	0	187	273	−0.101
42	4924.927	1.092	1.135	1.081	86	168	333	−0.330
42	5018.440	1.163	1.151	1.133	84	163	275	−0.444
42	5169.033	1.160	1.157	1.129	87	180	310	−0.508
43	4731.453	1.036	1.044	0	120	219	339	−0.141
48	5362.869	1.065	1.079	1.060	94	194	315	−0.245
49	5197.577	1.086	1.095	1.072	84	182	343	−0.290
49	5234.625	1.082	1.102	1.073	89	180	296	−0.281
49	5276.002	1.099	1.109	1.090	82	181	248	−0.322
49	5316.615	1.209	1.221	1.177	90	178	320	−0.326
55	5534.847	1.056	1.068	1.045	94	123	278	−0.287

Table 5. continued.

Multiplet	λ Å	I_b	I_r	I_{cd}	D_p (km s^{-1})	$D_{1/2}$ (km s^{-1})	D_1 (km s^{-1})	W_λ Å
73	7462.407	1.032	1.035	1.023	112	202	286	−0.149
73	7515.831	1.098	0	0	0	183	405	−0.470
73	7711.723	1.086	1.099	1.074	67	162	298	−0.389
74	6416.919	1.024	1.029	1.014	112	210	289	−0.098
74	6456.383	1.108	1.131	1.099	100	207	327	−0.522
HD 157042								
27	4233.172	1.033	1.018	1.016	494	656	782	−0.1934
27	4351.769	1.019	1.015	1.003	467	586	661	−0.1024
38	4583.837	1.031	1.016	0	486	536	637	−0.2093
42	4923.927	1.028	1.025	—	482	594	714	−0.1393
42	5018.440	1.033	1.036	—	406	614	704	−0.2745
42	5169.033	1.041	1.024	—	431	599	689	−0.2311
49	5316.615	1.043	1.013	—	484	572	668	−0.2160
HD 158427								
27	4233.172	1.041	1.021	1.011	244	431	628	−0.1642
27	4351.769	1.015	1.025	1.001	250	452	583	−0.0947
27	4416.830	1.012	1.017	1.004	237	440	567	−0.0723
37	4629.339	1.035	1.025	1.006	289	434	528	−0.1415
38	4583.837	1.052	1.061	1.034	223	424	646	−0.3458
42	4923.927	1.038	1.043	1.000	266	491	685	−0.2305
42	5018.440	1.055	1.070	1.014	257	448	668	−0.3694
42	5169.033	1.061	1.056	1.015	253	492	651	−0.3831
48	5362.869	1.020	1.024	1.011	281	549	613	−0.1521
49	5197.577	1.036	1.030	1.014	263	454	726	−0.2274
49	5234.625	1.029	1.029	1.011	223	449	580	−0.1736
49	5276.002	1.030	1.021	1.005	254	435	604	−0.1527
49	5316.615	1.081	1.067	1.040	233	442	638	−0.5056
73	7515.831	1.063	1.064	0	227	500	738	−0.7633
73	7711.723	1.026	1.038	1.014	244	432	537	−0.3073
74	6247.557	1.012	1.014	1.005	213	432	554	−0.0915

I_b, I_r, and I_{cd} = intensities of the blue, red peak, and central depression in the two-peaked emission profiles in units of the local continuum; D_p, $D_{1/2}$, and D_1 = separation of emission peaks, width of lines at half intensity and at intensity $I/I_c = 1.0$ in velocity units; W_λ: equivalent width.

Table 6. Measurements of the observed hydrogen Balmer emission lines.

HD	I_p	I_b	I_r	D_p	$D_{1/2}$	D_1	W_λ	W_{cd}	Npeaks
				km s^{-1}			Å	Å	
					Hα				
41335	0.000	4.188	3.593	197	464	1364	−31.155	0.331	2
45725	0.000	4.136	4.236	147	428	1446	−33.197	0.361	2
48917	0.000	3.725	3.795	107	337	1433	−23.665	0.110	2
50013	5.691	0.000	0.000	0	356	823	−28.292	0.000	1
56139	3.465	0.000	0.000	0	205	625	−10.731	0.000	1
58978	1.882	1.714	1.849	354	608	1500	−12.105	0.000	3
63462	0.000	2.177	1.992	182	499	1171	−12.623	0.117	2
88661	0.000	4.778	3.999	111	288	924	−23.970	0.156	2
91465	0.000	4.073	4.119	95	379	1385	−28.726	0.041	2
105435	—	—	—	—	—	—	—	—	—
110335	0.000	3.690	3.639	95	299	809	−18.628	0.146	2
112091	0.000	5.482	5.510	62	252	755	−26.243	0.031	2
120991	4.587	0.000	0.000	0	170	872	−16.174	0.000	1
124367	0.000	5.960	5.980	92	319	1324	−39.113	0.070	2
148184	11.000	0.000	0.000	0	151	1214	−42.838	0.000	1
157042	—	—	—	—	—	—	—	—	—
158427	0.000	4.694	4.477	124	389	1522	−33.478	0.121	2
164284	0.000	7.091	7.036	86	304	1031	−44.220	0.070	2
					Hβ				
41335	0.000	1.540	1.502	221	376	755	−2.901	0.294	2
45725	0.000	1.589	1.596	219	380	648	−3.155	0.457	2
48917	0.000	1.423	1.407	188	316	653	−2.091	0.165	2
50013	0.000	1.629	1.625	162	307	866	−3.325	0.101	2
56139	0.000	1.359	1.363	45	168	320	−1.008	0.004	2
58978	0.000	1.158	1.157	331	478	774	−0.956	0.299	2
63462	0.000	1.270	1.220	249	456	783	−1.778	0.094	2
88661	0.000	1.719	1.554	144	280	836	−3.084	0.170	2
91465	0.000	1.568	1.461	158	344	1094	−3.046	0.140	2
105435	0.000	1.934	1.715	117	251	730	−3.486	0.117	2
110335	0.000	1.398	1.392	176	314	625	−1.770	0.247	2
112091	0.000	1.418	1.417	135	290	573	−1.984	0.087	2
120991	2.147	0.000	0.000	0	108	344	−2.204	0.000	1
124367	0.000	1.547	1.571	208	349	890	−3.404	0.192	2
148184	2.981	0.000	0.000	0	133	646	−4.912	0.000	1
157042	0.000	1.283	1.443	220	391	802	−2.203	0.256	2
158427	0.000	1.492	1.429	192	378	825	−2.798	0.177	2
164284	0.000	1.681	1.769	153	320	740	−3.704	0.184	2
					Hγ				
41335	0.000	1.138	1.152	222	379	688	−0.623	0.181	2
45725	0.000	1.160	1.166	232	366	532	−0.498	0.318	2
48917	0.000	1.122	1.092	217	303	687	−0.366	0.163	2-3
50013	0.000	1.177	1.182	166	308	430	−0.704	0.099	2
56139	0.000	1.114	1.112	55	167	289	−0.280	0.005	2
58978	0.000	1.094	1.085	312	471	611	−0.457	0.202	2
63462	0.000	1.112	1.082	286	501	779	−0.597	0.089	2
88661	0.000	1.195	1.168	163	284	633	−0.687	0.127	2
91465	0.000	1.152	1.107	180	362	663	−0.585	0.082	2
105435	0.000	1.243	1.187	139	260	469	−0.753	0.080	2
110335	0.000	1.142	1.131	194	323	522	−0.497	0.143	2
112091	0.000	1.069	1.061	187	284	413	−0.201	0.073	2
120991	1.520	0.000	0.000	0	110	273	−0.872	0.000	1
124367	0.000	1.095	1.097	204	331	560	−0.384	0.115	2
148184	0.000	1.694	1.639	33	154	445	−1.619	0.000	2
157042	0.000	1.085	1.114	269	390	555	−0.365	0.186	2
158427	0.000	1.086	1.069	223	360	507	−0.307	0.121	2
164367	0.000	1.172	1.216	262	311	520	−0.772	0.120	2

Table 6. continued.

HD	I_p	I_b	I_r	D_p	$D_{1/2}$	D_1	W_λ	W_{cd}	Npeaks
				km s^{-1}			Å	Å	
					Hδ				
41335	0.000	1.063	1.074	251	0	621	−0.286	0.124	2
45725	0.000	1.041	1.031	289	0	0	−0.089	0.307	2
48917	0.000	1.109	1.055	244	404	688	−0.364	0.150	2-3
50013	0.000	1.098	1.059	197	317	477	−0.259	0.084	2
56139	0.000	1.048	1.048	84	176	287	−0.113	0.009	2
58978	0.000	1.043	1.050	307	490	560	−0.232	0.082	2
63462	0.000	1.086	1.039	358	521	732	−0.320	0.123	2
88661	0.000	1.067	1.080	195	313	599	−0.265	0.088	2
91465	0.000	1.052	1.011	200	0	381	−0.085	0.046	2
105435	0.000	1.090	1.070	155	276	458	−0.255	0.064	2
110335	0.000	1.076	1.070	209	377	632	−0.299	0.099	2
110335	0.000	1.076	1.070	209	377	632	−0.299	0.099	2
112091	0.000	1.050	1.039	204	356	461	−0.155	0.054	2
120991	1.310	0.000	0.000	0	121	263	−0.539	0.000	1
124367	0.000	1.037	1.030	208	317	433	−0.096	0.051	2
148184	0.000	1.379	1.339	44	171	481	−0.953	0.000	2
157042	0.000	1.070	1.062	273	399	555	−0.261	0.097	2
158427	0.000	1.050	1.040	238	363	563	−0.165	0.064	2
164284	0.000	1.054	1.061	207	324	505	−0.207	0.079	2

I_p, I_b, and I_r = intensities of the peak of one-peaked line profiles, the blue and red peak intensities of two-peaked line profiles; D_p, $D_{1/2}$, and D_1 = separation of emission peaks, width of lines at half intensity and at I/I_c = 1.0 in velocity units; W_λ = equivalent width; W_{cd} = equivalent width of the central depression; Npeaks = number of emission peaks.

Table 7. Atomic data of the sudied Fe II lines.

Multiplet	λ_o	log gf	E_l	E_u
27	4128.748	–3.470	2.583	5.585
27	4173.461	–2.513	2.583	5.553
27	4233.172	–1.836	2.583	5.511
27	4273.326	–3.258	2.704	5.605
27	4303.176	–2.443	2.704	5.585
27	4351.769	–2.130	2.704	5.553
27	4385.387	–2.542	2.778	5.605
27	4416.830	–2.534	2.778	5.585
28	4178.862	–2.785	2.583	5.549
28	4258.154	–3.799	2.704	5.615
28	4296.572	–3.198	2.704	5.589
37	4489.183	–3.422	2.828	5.589
37	4491.405	–2.684	2.856	5.615
37	4515.339	–2.467	2.844	5.589
37	4520.224	–2.983	2.807	5.549
37	4534.168	–3.253	2.856	5.589
37	4555.893	–2.325	2.828	5.549
37	4582.835	–3.094	2.844	5.549
37	4629.339	–2.306	2.807	5.484
37	4666.758	–3.221	2.828	5.484
38	4508.288	–2.312	2.856	5.605
38	4522.634	–2.119	2.844	5.585
38	4541.524	–2.847	2.856	5.585
38	4549.474	–1.957	2.828	5.553
38	4576.340	–2.822	2.844	5.553
38	4583.837	–1.802	2.807	5.511
43	4731.453	–3.053	2.891	5.511
42	4923.927	–1.559	2.891	5.408
42	5018.440	–1.400	2.891	5.361
42	5169.033	–1.303	2.891	5.289
49	5197.577	–2.233	3.230	5.615
49	5234.625	–2.151	3.221	5.589
49	5254.929	–3.227	3.230	5.589
49	5276.002	–2.073	3.199	5.549
49	5316.615	–1.930	3.153	5.484
49	5325.553	–3.220	3.221	5.549
49	5425.257	–3.372	3.199	5.484
41	5284.109	–3.299	2.891	5.237
48	5264.812	–3.303	3.230	5.585
48	5316.784	–2.908	3.221	5.553
48	5362.869	–2.739	3.199	5.511
55	5534.847	–2.996	3.245	5.484
74	6147.741	–2.721	3.889	5.905
74	6149.258	–2.724	3.889	5.905
74	6238.392	–2.630	3.889	5.876
74	6247.557	–2.329	3.892	5.876
74	6416.919	–2.740	3.892	5.823
74	6456.383	–2.075	3.903	5.823
40	6532.628	–3.708	2.891	4.818
43	7462.407	–2.734	3.892	5.553
73	7515.831	–3.432	3.903	5.553
73	7711.723	–2.543	3.903	5.511